Ocean Engineering 238 (2021) 109758

Contents lists available at ScienceDirect

Ocean Engineering

journal homepage: www.elsevier.com/locate/oceaneng

Space-time frequency spectra analyses of the unsteady cavitating vortical flows inside a mixed-flow pump

Renfang Huang [a,*], Rundi Qiu [a,b], Yiwei Wang [a,b,**], Xianwu Luo [c], Wei Zhang [d]

[a] Key Laboratory for Mechanics in Fluid Solid Coupling Systems, Institute of Mechanics, Chinese Academy of Sciences, Beijing, 100190, China
[b] School of Future Technology, University of Chinese Academy of Sciences, Beijing, 100049, China
[c] State Key Laboratory of Hydroscience and Engineering, Department of Energy and Power Engineering, Tsinghua University, Beijing, 100084, China
[d] Science and Technology on Water Jet Propulsion Laboratory, Shanghai, 200011, China

ARTICLE INFO

Keywords:
Mixed-flow pump
Pressure fluctuations
Cavitation
Wavelet analysis

ABSTRACT

The objective of this paper is to investigate the space-time frequency spectra for cavitating flows in a mixed-flow pump by using both fast Fourier transform and wavelet transform. Unsteady cavitating flows in a mixed-flow pump are numerically investigated by using the Reynolds-averaged Navier-Stokes method, which is closured with SST k-ω turbulence model and Zwart cavitation model. The cavitation performance is fairly predicted when compared with available experimental data. There are two stages for unsteady cavitation evolution during one impeller rotating cycle, including the cavity growth stage and diminution stage. The cavitation in the impeller is characterized by the spatial non-uniform distribution since a high-pressure region presents at the impeller inlet plane. The pressure amplitude decreases when the cavitation becomes severer at a smaller operating velocity. Besides, the dominant frequency in the impeller is the impeller rotating frequency (f_n), i.e. the cavity evolution frequency. Due to the rotor-stator interaction from the six-blade impeller, there is a dominant long-term frequency of $6f_n$ in the intake duct and the diffuser inlet. Furthermore, a broadband low-frequency around $1.5f_n$ exhibits near the diffuser exit, and the $1.5f_n$ amplitude varies over time corresponding to different corner-vortex dynamics. Therefore, wavelet analysis is a more favorable and practical method to obtain time-dependent frequency information for unsteady cavitating flows.

1. Introduction

The mixed-flow pump is a kind of pump with the performance and structure between the centrifugal pump and the axial-flow pump (Ji and Wang, 2011; Liu et al., 2016). It has many properties, such as small diameter, less floor area, high efficiency, and rapid start-up. With the modern advanced design technique, the mixed-flow pump can not only reach a high level of energy performance with the efficiency over 90% but also can be operated efficiently and stably in a wide range (Huang et al., 2019). Based on those advantages, the mixed-flow pump is broadly utilized in the water transfer projects, agricultural irrigation, urban water supply network, circulating water systems in power plants, and other fields (Li et al., 2020). For example, according to statistics of the Japan Turbo Machinery Association, the mixed-flow pump is over 93% among the circulating water pumps, which is provided by Japanese pump manufacturers for the thermal and nuclear power plants around the world from 2003 to 2006, and the maximum diameter is 4 m (Pan et al., 2012). However, when cavitation occurs in the pump, the unsteady cavitating flows would aggravate the flow instabilities, representing as flow separations, strong jet-wakes and complex vortex, which would cause a dramatic drop in the pump head and efficiency, and even induce noise and vibration. Therefore, the operational stability has become a prominent issue for the mixed-flow pump, especially under the off-design conditions. As an important evaluation index for the operational stability, pressure pulsations have become a research hotspot for scholars all over the world.

In recent years, many efforts have been made to investigate pressure fluctuations and flow instabilities at non-cavitating conditions. Ye et al. numerically studied flow instabilities inside a low-specific pump from the viewpoints of the Lagrangian coherent structure (LCS) and various vorticity dynamics, and found that the rotating stall cell would propagate in the circumferential direction with the frequency (f_{stall}) smaller

* Corresponding author.
** Corresponding author.
E-mail addresses: hrenfang@yeah.net (R. Huang), wangyw@imech.ac.cn (Y. Wang).

https://doi.org/10.1016/j.oceaneng.2021.109758
Received 9 February 2021; Received in revised form 17 July 2021; Accepted 27 August 2021
Available online 6 September 2021

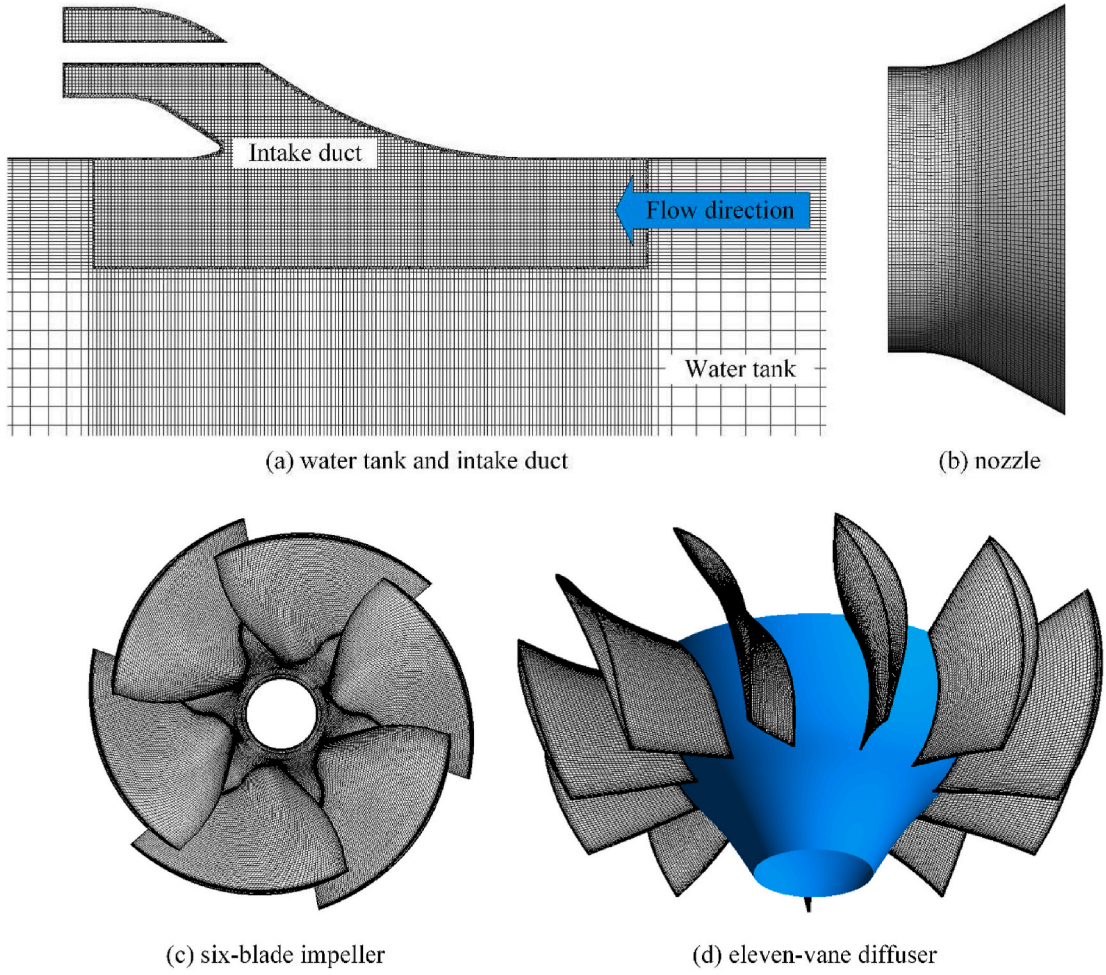

Fig. 1. The grid distributions in the computational domain (a) water tank and intake duct, (b) nozzle, (c) six-blade impeller, (d) eleven-vane diffuser.

Table 1
Operating conditions in this study.

	V_s (m/s)	n (r/min)	H (m)	Q (m^3/s)
Case 1	15	2806	44.74	0.599
Case 2	16	2807	44.48	0.604
Case 3	17	2809	44.10	0.609

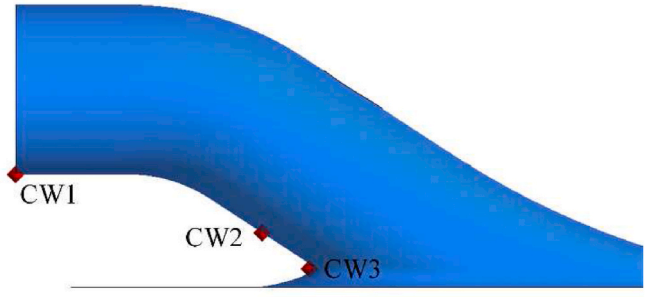

Fig. 2. Locations of monitoring points in the intake duct with point CW1∼CW3 along the lower wall.

than the impeller rotating frequency ($f_{stall} = 8.76\%f_n$) (Ye et al., 2019a, 2019b). Yang et al. reported that the rotating stall would block the flow passage and push the flow towards the leading edge of the subsequent guide vane (Yang et al., 2019). Pressure fluctuations of a mixed-flow

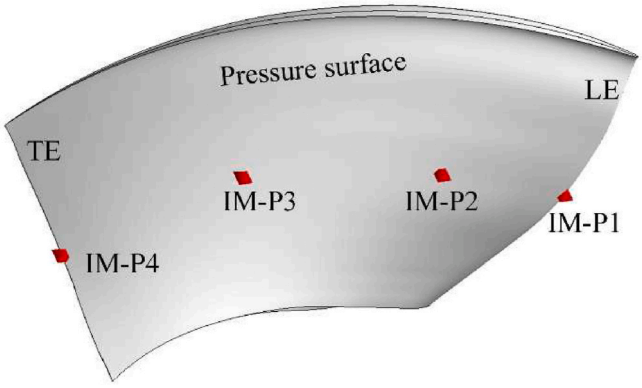

Fig. 3. Locations of the monitoring points on the impeller pressure surface.

waterjet pump were studied under a non-uniform inflow with different cruising speeds, revealing two dominant frequency components, i.e. one is induced by the rotor-stator interaction and the other is excited by an unsteady vortex in diffuser (Huang et al., 2020c; Luo et al., 2020). This is also studied for a mixed-flow pump under both design and off-design conditions (Xu et al., 2018), and then the dependence of the energy performance and pressure fluctuations on the blade rotational angle, the blade tip clearance, the inlet guide vane geometry and the wall roughness are extensively discussed in (Lei et al., 2017; Liu et al., 2018; Liu and Tan, 2018; Xu et al., 2017; Yao et al., 2018). Besides, great

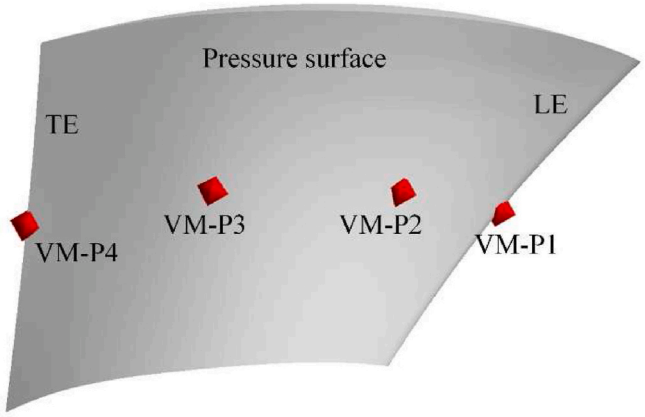

Fig. 4. Locations of the monitoring points on the diffuser pressure surface.

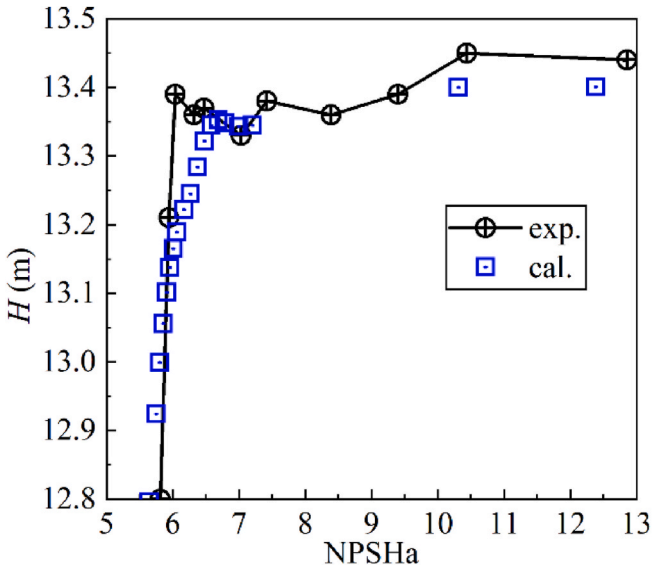

Fig. 5. Comparisons of the cavitation characteristics between calculations (abbreviated as cal.) and experiments (abbreviated as exp.).

attention has been paid to the pressure fluctuations and flow patterns in the reversible pump-turbine. Zhang et al. systematically studied the pressure pulsations in a pump-turbine under various operating modes and explained the correlations among various flow patterns, indicating that pressure pulsations under the turbine mode were mostly impacted by the opening angle of the guide vane (Zhang et al., 2020). Yang et al. (2020) described the unsteady flow features and pressure pulsations in a prototype pump-turbine during the runaway process, demonstrating that the flow patterns are strongly related to the runner velocity triangles which depend on the discharge and the rotational speed.

At present, there are a few studies about pressure fluctuations in a pump under cavitation conditions, while a vast majority of research work focuses on the hydraulic turbine, hydrofoil, etc. Yu et al. (2020) investigated pressure pulsations in a hydraulic turbine and found two types of pressure pulsations, i.e., one is resulted from the rotating vortex rope and the other is due to cavitation volume surge. Besides, some suggestions are proposed to suppress the cavitation excited pressure pulsations, like air admission (Huang et al., 2014), runner modification (Yu et al., 2019), overhanging grooves (Cheng et al., 2020). Huang et al. experimentally explored the effects of vortex generator on the propeller cavitation and hull pressure fluctuations, indicating that the vortex generator with proper geometry and installed location can make the cavitation variation mild and decrease the pressure fluctuations (Huang et al., 2020a). Hao and Tan (2018) compared different types of tip clearances on the cavitation performance for a mixed-flow pump and they found that dominant frequencies of the radial force are related to the blade number and the guide vane number.

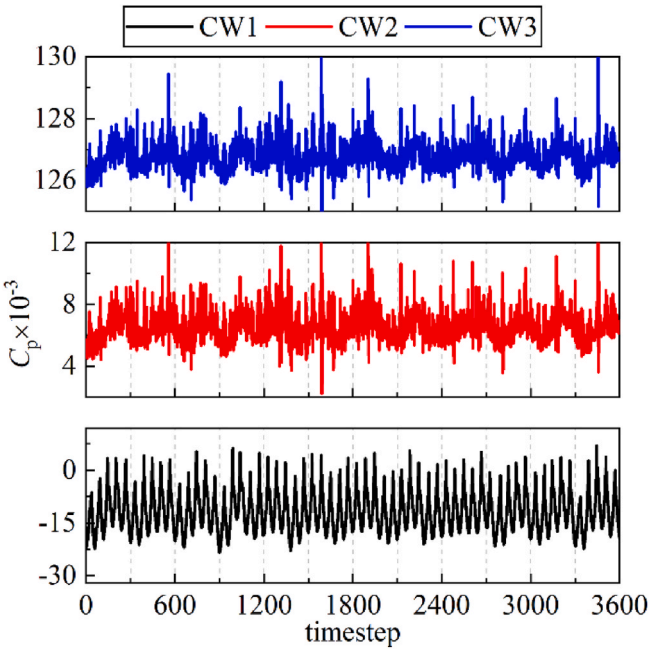

Fig. 6. Time histories of three monitoring points (CW1, CW2, CW3) located at the lower wall of the intake duct at $V_s = 17$ m/s (Case 3).

The transient pressure data can be obtained via experiments or numerical simulations, the key issue is how to analyze and evaluate the pressure fluctuations. Apart from the time-dependent pressure signals, Fast Fourier Transform (FFT) is usually applied to identify the frequency information. Venning et al. (2018) used the FFT method to extract individual pixel intensities in high-speed images for cloud cavitation, and they found three frequencies, i.e., the main shedding mode, the subharmonic mode and the harmonic model. The cavitating flows are characterized by strong unsteadiness, so the continuous wavelet transformations (CWT) is adopted by Kolahan et al. (2019) to analyze the oscillated frequency spectral content for the cloud cavitation over a sphere. Wu et al. (2017) applied the Complex Morlet Wavelets to analyze the cavitating flow-induced vibration of a stainless steel hydrofoil at various cavitation regimes. They found that the flow-induced frequency agrees well with the cavity shedding frequency, which is decreased along with the cavitation number due to a longer cavity and larger evolution cycle. Brandner et al. (2018) also used the CWT method to a diverse set of experiments, such as the turbulent bubble break-up.

The mixed-flow pump is an important apparatus in the marine energy utilization engineering, and its operating stability is of great significance to the offshore platform and the renewable energy system. As the above literature review indicates, a few studies have been conducted on the pressure fluctuations of unsteady cavitating vortical flows inside a mixed-flow pump. On the other hand, there is no systematic research about the correlation between cavitating flow patterns and pressure fluctuations. Therefore, this paper is thrown on the space-time frequency spectra for cavitating flows in a mixed-flow pump by using both wavelet and Fast Fourier Transforms.

2. Numerical simulation

2.1. Governing equations

The unsteady cavitating flows are governed by the Reynolds-

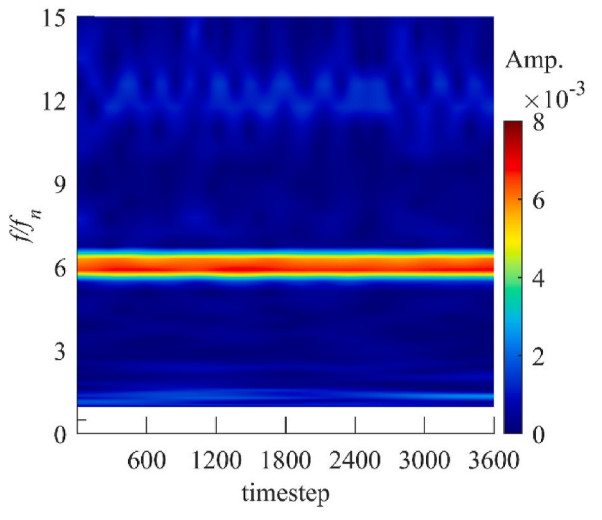

(a) CW1

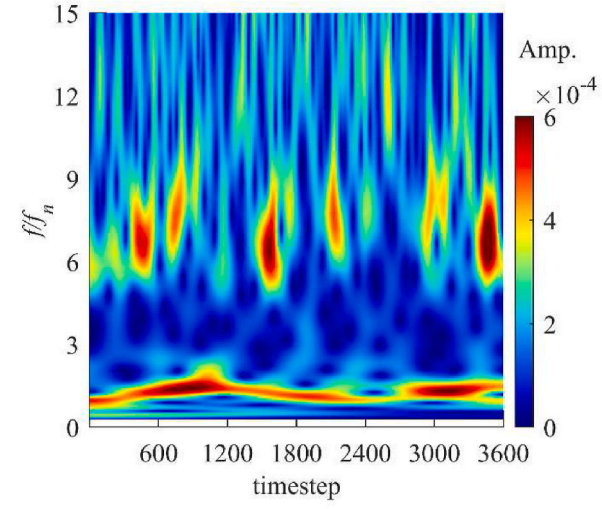

(b) CW2

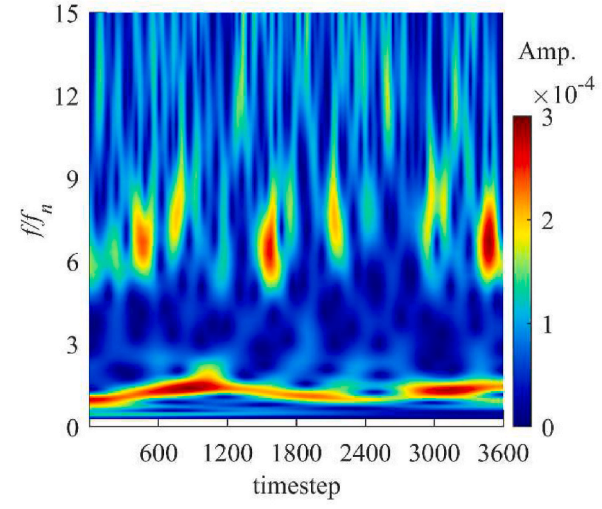

(c) CW3

Fig. 7. Time-dependent frequency spectra in the intake duct (CW1, CW2, CW3) at $V_s = 17$ m/s (Case 3).

averaged Navier-Stokes (RANS) equations in the framework of homogeneous assumption, which is both liquid phase and vapor phase share the same pressure and velocity fields. The incompressible continuity and momentum equations are given in equation (1) ~ (2), where p is the mixture pressure, u_i is the i-th velocity, μ is the laminar viscosity, μ_t is the turbulent eddy viscosity, ρ_m is the mixture density given in equation (3). Subscript v and l denote the vapor phase and the liquid phase, respectively. α_v is the vapor volume fraction.

$$\frac{\partial \rho_m}{\partial t} + \frac{\partial}{\partial x_j}(\rho_m u_j) = 0 \tag{1}$$

$$\frac{\partial}{\partial t}(\rho_m u_i) + \frac{\partial}{\partial x_j}(\rho_m u_i u_j) = -\frac{\partial p}{\partial x_i} + \frac{\partial}{\partial x_j}\left[(\mu + \mu_t)\left(\frac{\partial u_i}{\partial x_j} + \frac{\partial u_j}{\partial x_i} - \frac{2}{3}\frac{\partial u_k}{\partial x_k}\delta_{ij}\right)\right] \tag{2}$$

$$\rho_m = \alpha_v \rho_v + (1 - \alpha_v)\rho_l \tag{3}$$

In this work, the turbulent eddy viscosity μ_t is closured by the SST k-ω turbulence model which is accurate and reliable for many various kinds of flows, such as adverse pressure gradient flows, hydrofoils, transonic shock waves (Menter, 1994). The SST k-ω turbulence model is given as follows,

$$\frac{\partial}{\partial t}(\rho_m k) + \frac{\partial}{\partial x_i}(\rho_m k u_i) = \frac{\partial}{\partial x_j}\left[\left(\mu + \frac{\mu_t}{\sigma_k}\right)\frac{\partial k}{\partial x_j}\right] + P_k - \beta^* \rho_m k\omega \tag{4}$$

$$\frac{\partial}{\partial t}(\rho_m \omega) + \frac{\partial}{\partial x_i}(\rho_m \omega u_i) = \frac{\partial}{\partial x_j}\left[\left(\mu + \frac{\mu_t}{\sigma_\omega}\right)\frac{\partial \omega}{\partial x_j}\right] + \gamma\frac{\omega}{k}P_k - \beta\rho_m\omega^2 + 2(1 - F_1)\frac{\rho_m}{\omega\sigma_{\omega 2}}\frac{\partial k}{\partial x_j}\frac{\partial \omega}{\partial x_j} \tag{5}$$

where P_k represents the production of turbulence kinetic energy; σ_k and σ_ω is the turbulent Prandtl numbers for k and ω, respectively, described in equation (6) ~ (7) with model constants in equation (8).

$$\sigma_k = \frac{1}{F_1/\sigma_{k1} + (1 - F_1)/\sigma_{k2}} \tag{6}$$

$$\sigma_\omega = \frac{1}{F_1/\sigma_{\omega 1} + (1 - F_1)/\sigma_{\omega 2}} \tag{7}$$

$$\sigma_{k1} = 1.176, \sigma_{k2} = 1, \sigma_{\omega 1} = 2, \sigma_{\omega 2} = 1.168 \tag{8}$$

The blending function F_1 in equations (6) and (7) is provided in equations (9) and (10), where y is the distance to the next surface and D_ω^+ is the positive portion of the cross-diffusion term.

$$F_1 = \tanh\left(\Phi_1^4\right), \quad \Phi_1 = \min\left[\max\left(\frac{\sqrt{k}}{0.09\omega y}, \frac{500\mu}{\rho_m y^2 \omega}\right), \frac{4\rho_m k}{\sigma_{\omega 2} D_\omega^+ y^2}\right] \tag{9}$$

$$D_\omega^+ = \max\left[2\rho_m \frac{1}{\sigma_{\omega 2}}\frac{1}{\omega}\frac{\partial k}{\partial x_j}\frac{\partial \omega}{\partial x_j}, 10^{-10}\right] \tag{10}$$

Coefficient γ is given in equations (11)–(13), where $\gamma_0 = 1/9$, $R_\omega = 2.95$, $\gamma_{i1} = 0.55$, $\gamma_{i2} = 0.44$.

$$\gamma = \gamma_\infty\left(\frac{\gamma_0 + Re_t/R_\omega}{1 + Re_t/R_\omega}\right) \tag{11}$$

$$\gamma_\infty = F_1\gamma_{i1} + (1 - F_1)\gamma_{i2} \tag{12}$$

$$Re_t = \frac{\rho_m k}{\mu\omega} \tag{13}$$

For incompressible flows, the term β^* in equation (4) is defined in equation (14), where Re_t is given by equation (13).

$$\beta^* = \beta_\infty^*\left(\frac{4/15 + \left(Re_t/R_\beta\right)^4}{1 + \left(Re_t/R_\beta\right)^4}\right) \tag{14}$$

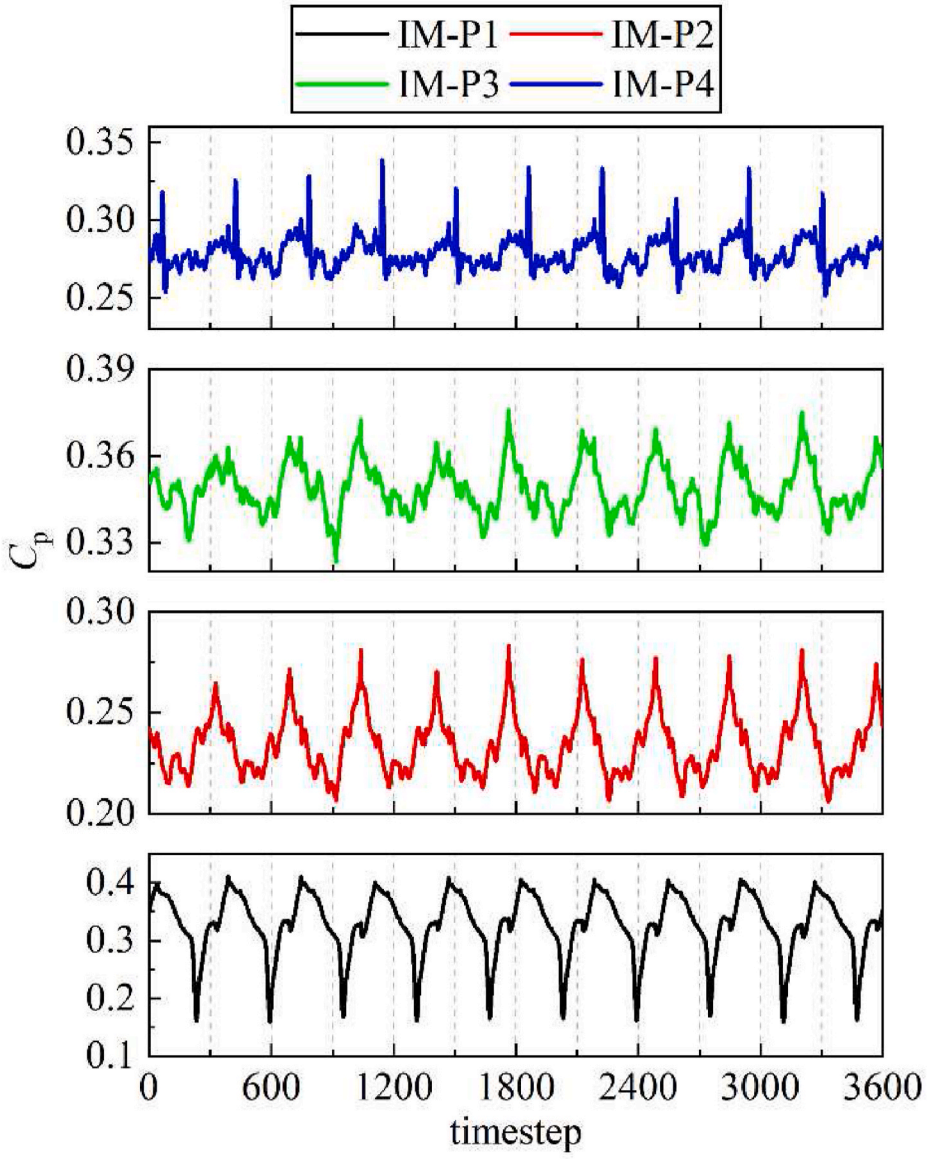

Fig. 8. Time histories of four monitoring points in the midspan of the impeller blade at $V_s = 17$ m/s (Case 3).

$$\beta_\infty^* = 0.09, \quad R_\beta = 8 \tag{15}$$

The term β in equation (5) is given by equations (16) and (17).

$$\beta = F_1\beta_{i1} + (1 - F_1)\beta_{i2} \tag{16}$$

$$\beta_{i1} = 0.075, \beta_{i2} = 0.0828 \tag{17}$$

Finally, the turbulent viscosity μ_t is obtained in equation (18) by a limiter to the formulation of the eddy viscosity to avoid the over-prediction, where S is the strain rate magnitude, the blending function F_2 is given in equation (19), model constant $a_1 = 0.31$.

$$\mu_t = \frac{\rho_m k}{\omega} \frac{1}{\max\left[1, \frac{SF_2}{a_1\omega}\right]} \tag{18}$$

$$F_2 = \tanh\left(\Phi_2^2\right), \Phi_2 = \max\left[2\frac{\sqrt{k}}{0.09\omega y}, \frac{500\mu}{\rho_m y^2 \omega}\right] \tag{19}$$

In order to make the vapor volume fraction α_v in equation (3) conservative, the Zwart's cavitation model (Zwart et al., 2004) is adopted to closure the mass transfer process which is given by equation (20) ~ (22), where F_{vap} and F_{cond} is an empirical factor for vaporization and condensation, respectively, and R_{nuc} is the nucleation site radius, r_{nuc} is the volume fraction of the nucleation site. The cavitation model constants are recommended in equation (23), which are extensively validated through experimental data and numerical simulations (Bardina et al., 1997; Luo et al., 2016).

$$\frac{\partial}{\partial t}(\rho_v\alpha_v) + \frac{\partial}{\partial x_i}(\rho_v\alpha_v u_i) = \dot{m}^+ - \dot{m}^- \tag{20}$$

$$\dot{m}^+ = F_{vap}\frac{3r_{nuc}(1-\alpha_v)\rho_v}{R_{nuc}}\sqrt{\frac{2}{3}\frac{\max(p_v - p, 0)}{\rho_l}} \tag{21}$$

$$\dot{m}^- = F_{cond}\frac{3\alpha_v\rho_v}{R_{nuc}}\sqrt{\frac{2}{3}\frac{\max(p - p_v, 0)}{\rho_l}} \tag{22}$$

$$F_{vap} = 50, F_{cond} = 0.01, \quad r_{nuc} = 5 \times 10^{-4}, R_{nuc} = 1 \times 10^{-6}\text{m} \tag{23}$$

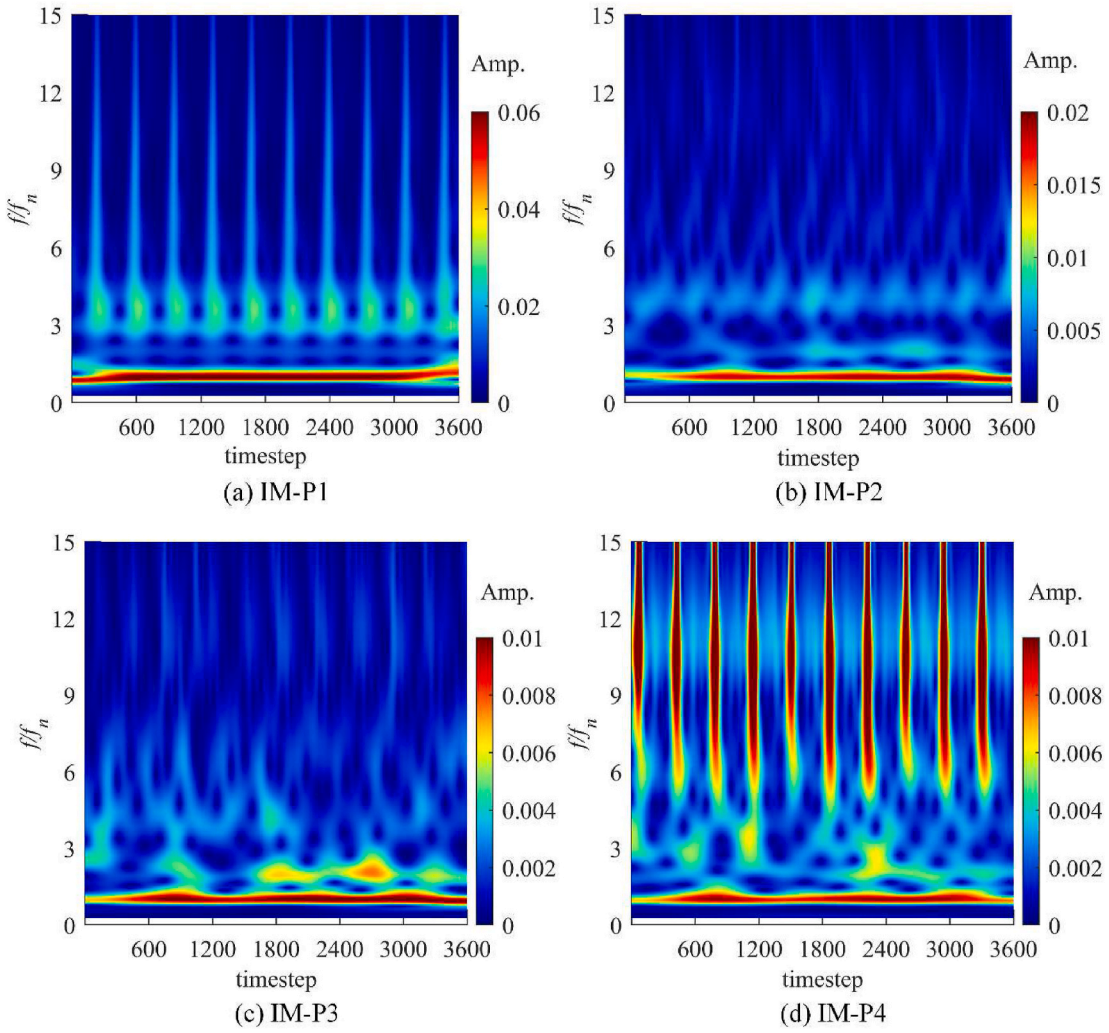

Fig. 9. Time-dependent frequency spectra of four monitoring points in the midspan of the impeller blade at $V_s = 17$ m/s (Case 3).

2.2. Frequency spectrum analysis

In this study, two common methods in signal processing are used to analyze pressure fluctuations obtained from numerical simulations, that is Fast Fourier Transform (FFT) and Wavelet Transform. Benefited from the usage of digital technology, FFT is a popular method which can extract the temporal spectrum from original data and identify the dominant frequency. $f = f(x)$ is the expression with respect to the variable x at the point w, and can be taken the Fourier transform as defined in equation (24),

$$F(w) = c \int_{-\infty}^{\infty} f(x) e^{iswx} dx \tag{24}$$

where c and s are parameters of Fourier transform. Generally, $c = 1$ and $s = -1$. To perform the Fourier transform in computer, Discrete Fourier Transform (DFT) is defined in equation (25),

$$F(k) = \sum_{n=0}^{N-1} F(n) e^{-i(2\pi/N)kn}, k = 0, 1, \ldots, N-1 \tag{25}$$

DFT performs $O(N^2)$ operations, so it is expensive when N is large. To reduce the cost in DFT, Fast Fourier Transform (FFT) is introduced, which only performs $O(N \cdot \log N)$ operations.

Since Fourier transform is not applicable when the signal is not stationary stochastic, researchers replace the kernel function from trigonometric function to wavelet function and provide the continuous wavelet transforms (CWT) (Lilly and Olhede, 2009).

$$WT(a, \tau) = \frac{1}{\sqrt{a}} \int_{-\infty}^{\infty} f(t) \phi\left(\frac{t-\tau}{a}\right) dt, a > 0, \tau > 0 \tag{26}$$

where a, τ, ϕ is the scale, translation and mother wavelet, respectively. Scale corresponds to frequency. Larger scale can capture higher frequency. Wavelet transform can refine the signal by performing scale operation and translation operation. After multiplying original functions by mother wavelet, frequencies over time are obtained. Mother wavelet have the following properties: (i) ϕ (t) should be attenuated exponentially when x approaches positive or negative infinity; (ii) the integral of ϕ (t) from negative infinity to positive infinity is a constant; (iii) the mean value of ϕ (t) is zero.

Different types of mother wavelet can be used to calculate the time-varying frequency spectra. In this study, the analytic bump wavelet is adopted to analyze the sampled pressure fluctuations. The Fourier transform of the analytic bump wavelet with parameters χ and ξ is in equation (27),

$$\widehat{\phi}(\omega) = \exp\left(1 - \frac{1}{1 - \frac{(\omega-\chi)^2}{\xi^2}}\right) \cdot I_{(\chi-\xi, \chi+\xi)} \tag{27}$$

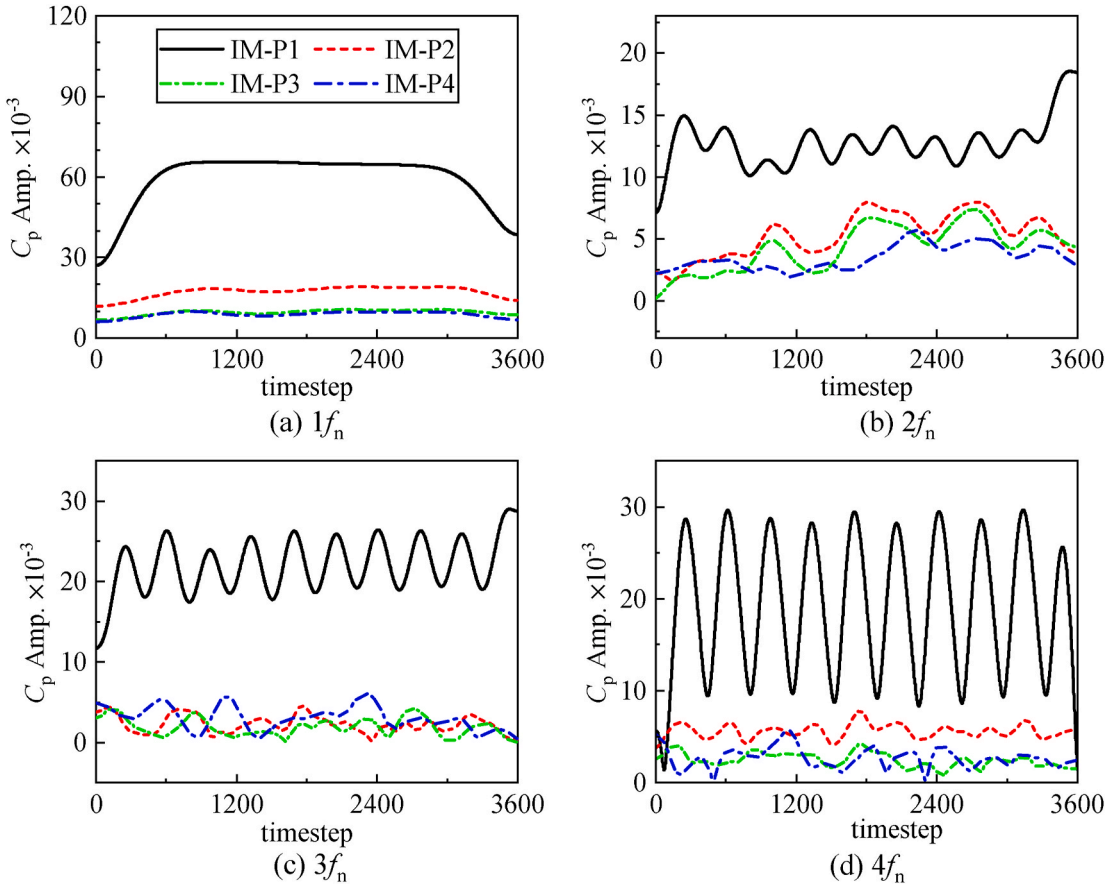

Fig. 10. Time histories of (a) 1f_n, (b) 2f_n, (c) 3f_n and (d) 4f_n at four monitoring points in the midspan of the impeller blade at V_s = 17 m/s (Case 3).

where $\widehat{\phi}(\omega) = \int_{-\infty}^{\infty} \phi(t)e^{-i\omega t}dt$. $I_{(\chi-\xi,\chi+\xi)}$ is an indicator function defined in equation (28)

$$I_{(\chi-\xi,\chi+\xi)} = \begin{cases} 1, & \chi-\xi \le \omega \le \chi+\xi \\ 0, & \text{other} \end{cases} \tag{28}$$

These parameters in bump wavelet are automatically adjusted according to the sampled data. Valid values for χ are ranging from 3 to 6, and valid values for ξ are ranging from 0.1 to 1.2. Smaller ξ value would obtain a wavelet with better frequency localization but worse time localization. On the other hand, larger ξ values would get a wavelet with preferable time localization and worse frequency localization.

Next, mother wavelet function is given in equation (29) for the convenience of calculation.

$$\widetilde{\phi}_a(t) = \frac{1}{\sqrt{a}}\phi\left(-\frac{t}{a}\right) \tag{29}$$

Continuous function is not practical to solve in computer, and hence a discrete form of CWT is derived. If we assume that $f(t)$ is a vector $\mathbf{x}[n]$ containing n elements, equation (26) can be expressed by,

$$\mathbf{WT}_a[\tau] = \sum_{n=0}^{N-1} \mathbf{x}[n]\widetilde{\phi}_a[\tau-n] \tag{30}$$

Finally, the time-dependent frequency spectrum is obtained. Note that scale cannot represent real frequency, so a relationship between the central frequency of mother wavelet (f_c) and the pseudo-frequency (f_a) is provided in equation (31).

$$f_a = \frac{f_c}{a \times dT} \tag{31}$$

where dT is the sampling period in vector $\mathbf{x}[n]$. Wavelet transform not only captures the frequency properties, but also provides the behavior of original function over time. Therefore, wavelet transform is widely applied in the signal multiresolution analyses.

2.3. Problem description

A mixed-flow pump is treated to numerically predict the unsteady cavitating flows. The computational domain is made up of a six-blade mixed-flow impeller, an eleven-vane diffuser, a nozzle, a large water tank together with an intake tank. The water tank is over 30D in length and has a rectangular cross-section of 10D (width) × 8D (height), where D is the diameter of the impeller inlet with the value of D = 244 mm. The geometrical parameters for the meridional passage, the impeller together with the intake duct are described in the literature (Huang et al., 2019).

Fig. 1 shows the grid distributions in each component. The structured grids are generated in the impeller, the diffuser, the nozzle and the water tank. On the other hand, the unstructured grids are used in the intake duct and the prism grids are applied close to the wall to guarantee yplus <50. For the purpose of evaluating numerical uncertainty, the grid independence is examined by using convergence index (GCI) (Roache, 1993), which has been assessed over a large number of cases and acknowledged as the most reliable and recommended method (Eça et al., 2005, 2007; Huang et al., 2020b). As a result, the grid elements for the final mesh are about 14 million based on our previous study (Huang et al., 2020c).

In this paper, the transient cavitating flows are solved under three operating conditions as shown in Table 1, which are selected from the navigational characteristic map when the input power is 310.4 kW. An operating velocity (V_s) in Table 1 is set at the inlet plane of the water tank with the hull boundary layer taken into account as described in

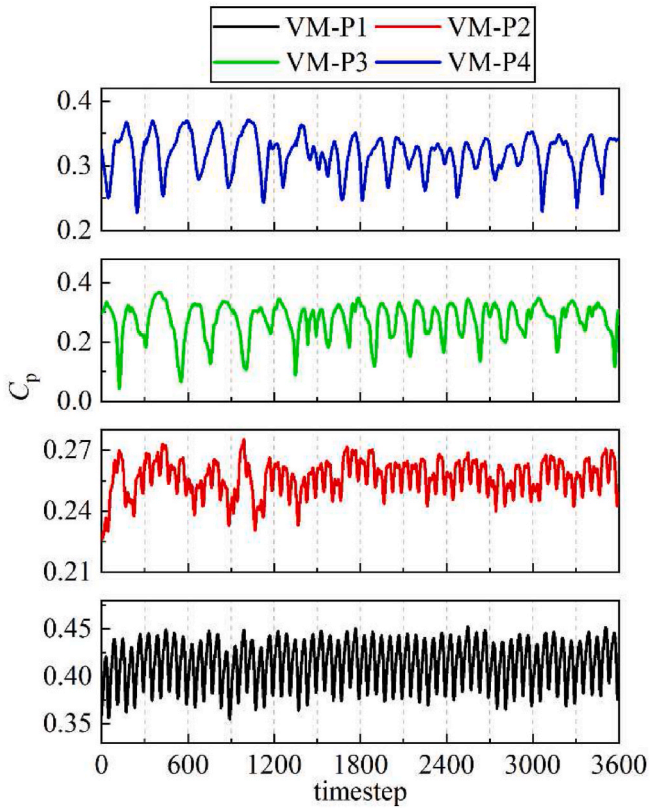

Fig. 11. Time histories of four monitoring points in the midspan of the diffuser vane at $V_s = 17$ m/s.

(Huang et al., 2020c). The rotational speed (n) in Table 1 is applied to the impeller, then the sliding mesh technique is used between the rotational impeller and the stationary component, i.e. the diffuser as well as the intake duct. The averaged static pressure is set at the outlet plane of the computational domain.

The direct coupling method is used for the present unsteady numerical simulations (Vanka, 1986). Convection terms are set as the high-order resolution scheme, diffusion terms are set as the central difference scheme, and the transient term is set as the unsteady second-order backward Euler formation (Huang et al., 2020c). The timestep corresponds to 1° per step which is sufficiently small for predicting the cavitation variation cycle in the impeller.

The instantaneous pressure is sampled every timestep at several monitoring points as shown in Figs. 2–4. The points CW1 ~ CW3 are located along the lower wall of the intake duct, the points IM-P1 ~ IM-P4 are located at the pressure surface of the impeller, and the points VM-P1 ~ VM-P4 are set at the pressure surface of the diffuser. Note that the monitoring points in the impeller would rotate along with the impeller blade. Subsequently, both continuous wavelet transformations (CWT) and fast Fourier transform (FFT) are used to obtain the space-time frequency spectra of the sampled pressure data combined with the transient cavity patterns.

3. Results and discussion

3.1. Validation

To validate the present simulation approach, the simulated results of cavitating flows are compared with the experimental results, which have been conducted in the laboratory of the Marine Design and Research Institute of China (Huang et al., 2020c). Experimental tests for cavitation performance have been conducted at the flow rate of $Q = 0.4505$ m^3/s, a rotational speed of $n = 1450$ r/min with gradually decreasing the inlet pressure. Therefore, the cavitation characteristics are defined by the available net positive suction head ($NPSH_a$) in equation (32), where p_{in} and v_{in} represent the static pressure and velocity at the inlet, respectively, p_v is the saturation vapor pressure of water at 25 °C, and g is the gravity acceleration with the value of 9.8 m/s^2 (Huang et al., 2015).

$$\mathrm{NPSH_a} = \left(\frac{p_{in}}{\rho g} + \frac{v_{in}^2}{2g}\right) - \frac{p_v}{\rho g} \tag{32}$$

The cavitation characteristics are compared between calculations and experiments for the model pump, as shown in Fig. 5. The head for the model pump gradually descends with decreasing the available net positive suction head ($NPSH_a$). Further decreasing the $NPSH_a$ to a certain value, the head is suddenly broken down. It is observed that the dependence of the pump head on the cavitation is reasonably predicted by the present numerical approach when compared to the experiments. Usually, the $NPSH_a$ value corresponding to the point where the pump head (i.e. H) drops by 3% is denoted as the critical $NPSH_a$. At present, the value of 3% dropping in the pump for both experiments and simulations is $H = 13.0$ m, the critical $NPSH_a$ is 5.827 m for experiments and 5.804 m for numerical simulations, and thus the relative error is 0.39%, demonstrating the present numerical approach is reliable to predict the cavitating flows in the mixed-flow pump.

3.2. Space-time frequency spectrum analyses

The pressure fluctuations would cause noise, structural vibrations, and even induce resonance when its frequency is equal to the natural frequency, so this is a problem to the operation stability and may result in huge economic losses. Therefore, it is of great importance to study the frequency spectra of cavitating flows in the mixed-flow pump. Current simulations for each case are performed for approximately 25 rotation cycles. In this work, flow statistics are sampled about 25 rotation cycles with the initial flow data corresponding to about 15 cycles rejected, and therefore Fast Fourier Transform and Wavelet transform are taken for the following 10 rotation cycles corresponding to 3600 data. Considering the unsteadiness of rotating cavitating flows, the CWT method together with FFT is applied to illustrate the time-dependent frequency spectra in the three-dimensional pump. For Case 3 in Table 1 ($V_s = 17$ m/s), the impeller rotating frequency is $f_n = 46.81$ Hz, so FFT resolution is approximately $0.1f_n$ for the present setup, which are much smaller than the dominant and harmonic frequencies. It is indicated that the frequency spectra are reliable based on the present sampled flow statistics.

Furthermore, the pressure coefficient C_p, a non-dimensional parameter, is defined in equation (33) to facilitate comparisons between different cases and monitoring points. In equation (33), p_i is the static pressure at the i-th monitoring point, p_r is the reference pressure for each case, u_2 is the circumferential velocity at the exit of the impeller blade tip.

$$C_p = \frac{p_i - p_r}{0.5\rho_l u_2^2} \tag{33}$$

3.2.1. Intake duct

Fig. 6 shows the time histories of three monitoring points located at the lower wall of the intake duct at $V_s = 17$ m/s (Case 3). The variation range of point CW1 is much larger than that of point CW2 and CW3. Fig. 7 shows the time-dependent frequency spectra of the point CW1 ~ CW3. It is observed the amplitude of the pressure coefficient is gradually decreased in the streamwise direction, that is, the amplitude of the pressure fluctuation from the smallest to the largest is CW3 < CW2 < CW1. From Fig. 7(a), the dominant frequency is around $6f_n$ at the point CW1, which is six times the impeller rotating frequency (f_n), and this is caused by the rotor-stator interaction (RSI) between the stationary duct and the rotating six-blade impeller. Moreover, the RSI effect still works

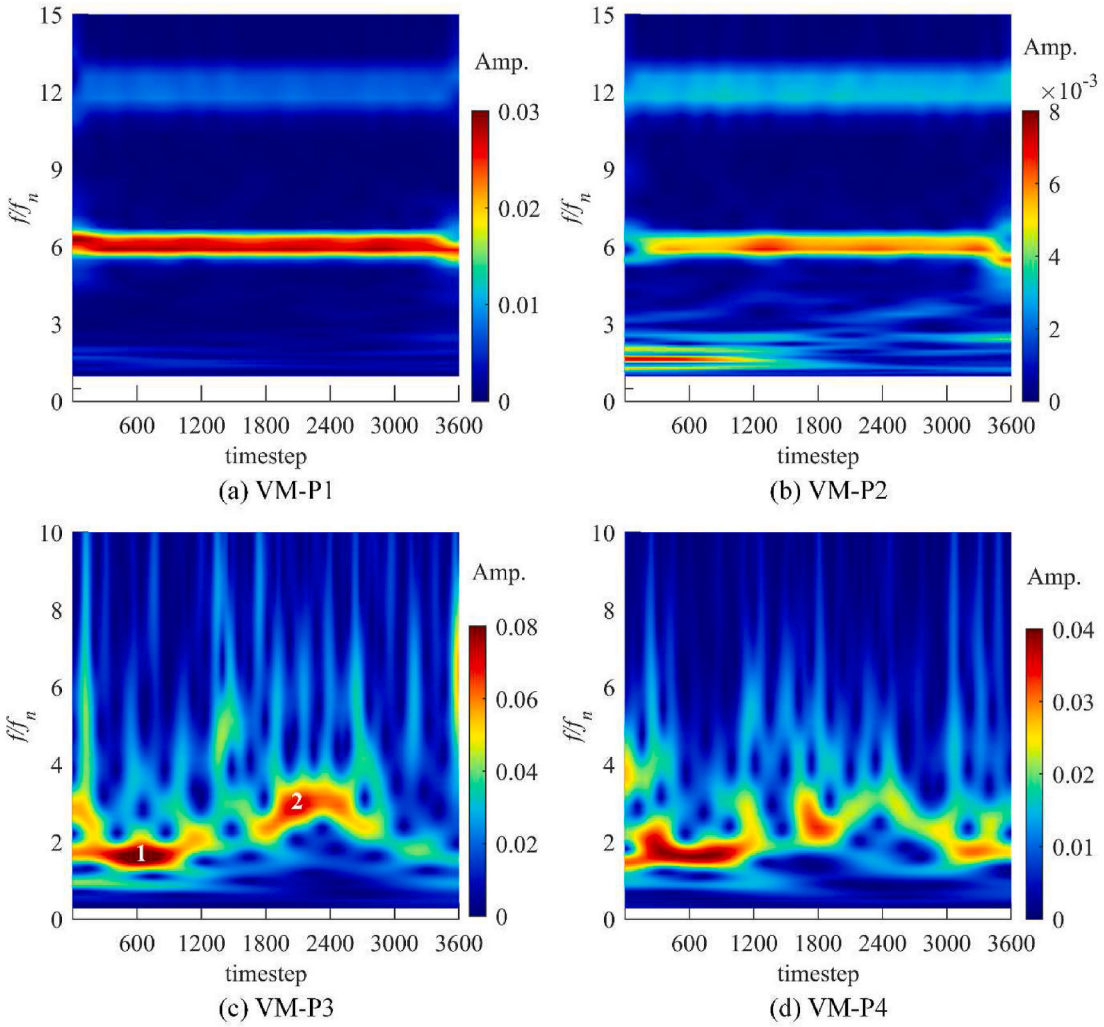

Fig. 12. Time-dependent frequency spectra of four monitoring points in the midspan of the diffuser vane at V_s = 17 m/s (Case 3).

at the point CW2 and CW3 having a $6f_n$ component, which is damped as the distance to the impeller becomes further. It is noted that $6f_n$ component is short-term at the point CW2 and CW3, while it is a long-term component at the point CW1. In contrast, there is a broadband low-frequency component at the point CW2 and CW3 with the value around $1.5f_n$.

3.2.2. Impeller

Fig. 8 shows the time histories of four monitoring points whose locations are in the midspan of the impeller blade for Case 3 in Table 1 (V_s = 17 m/s). It is in the downstream direction from the point IM-P1 to IM-P4, where IM is short for the *impeller*. Fig. 9 shows the time-dependent frequency spectra of the point IM-P1 ~ IM-P4, indicating that the dominant frequency is a long-term component with the value of the impeller rotating frequency (f_n). It is because that the monitoring points are located in the rotating impeller and the intake duct is stationary at the upstream of the impeller, from a relative perspective, the dominant frequency in the midspan of the impeller blade is the impeller rotating frequency (f_n), which is caused by the interaction between the intake duct and the rotating impeller. Note that the f_n amplitude is gradually decreased in the streamwise direction.

Besides, a short-term component of $11f_n$ is presented periodically at the point IM-P4, which is located at the blade trailing edge and close to the 11-vane diffuser. Thus, this $11f_n$ component is resulted from the rotor-stator interaction between the impeller and the diffuser.

In addition, several harmonic frequencies (i.e. $2f_n$ ~ $4f_n$) are also visible at the point IM-P1 ~ IM-P4, and their amplitudes are varied over time as shown in Fig. 10.

Based on the wavelet analysis, sorting the $2f_n$ amplitude from largest to smallest when the timestep >1200, the corresponding monitoring points are respectively in order as IM-P1 > IM-P2 > IM-P3 > IM-P4. That is, the $2f_n$ amplitude gradually decreases along with the flow direction. As shown in Fig. 10(c), the $3f_n$ amplitude is very close at IM-P2, IM-P3 and IM-P4, its largest amplitude is located at IM-P1. As for the harmonic frequency of $4f_n$, in general, its largest amplitude is at IM-P1, the second is located at IM-P2, and the amplitude is similar at IM-P3 and IM-P4.

3.2.3. Diffuser

Fig. 11 shows the pressure variations over time at the point VM-P1 ~ VM-P4 whose locations are in the midspan of the diffuser vane at V_s = 17 m/s (Case 3). It is in the downstream direction from VM-P1 to VM-P4. Fig. 12 shows the time-dependent frequency spectra of those monitoring points. Since the point VM-P1 and VM-P2 are close to the impeller exit, the rotor-stator interaction effect excited from the impeller still works. Consequently, the $6f_n$ component together with $12f_n$ is observed at VM-P1 and VM-P2, and the dominant frequency is the $6f_n$ component. There is a broadband low-frequency at the point VM-P2 during timestep = 0–1200. For the point VM-P3 and VM-P4, the frequency component is complex and varied over time. The broadband low-frequency at VM-P2 is obviously enlarged at VM-P3 and VM-P4, and its central frequency is around $1.5f_n$, labeled *dynamics 1*. Besides, another broadband frequency is observed around $3f_n$ at the point VM-P3 when the timestep is around

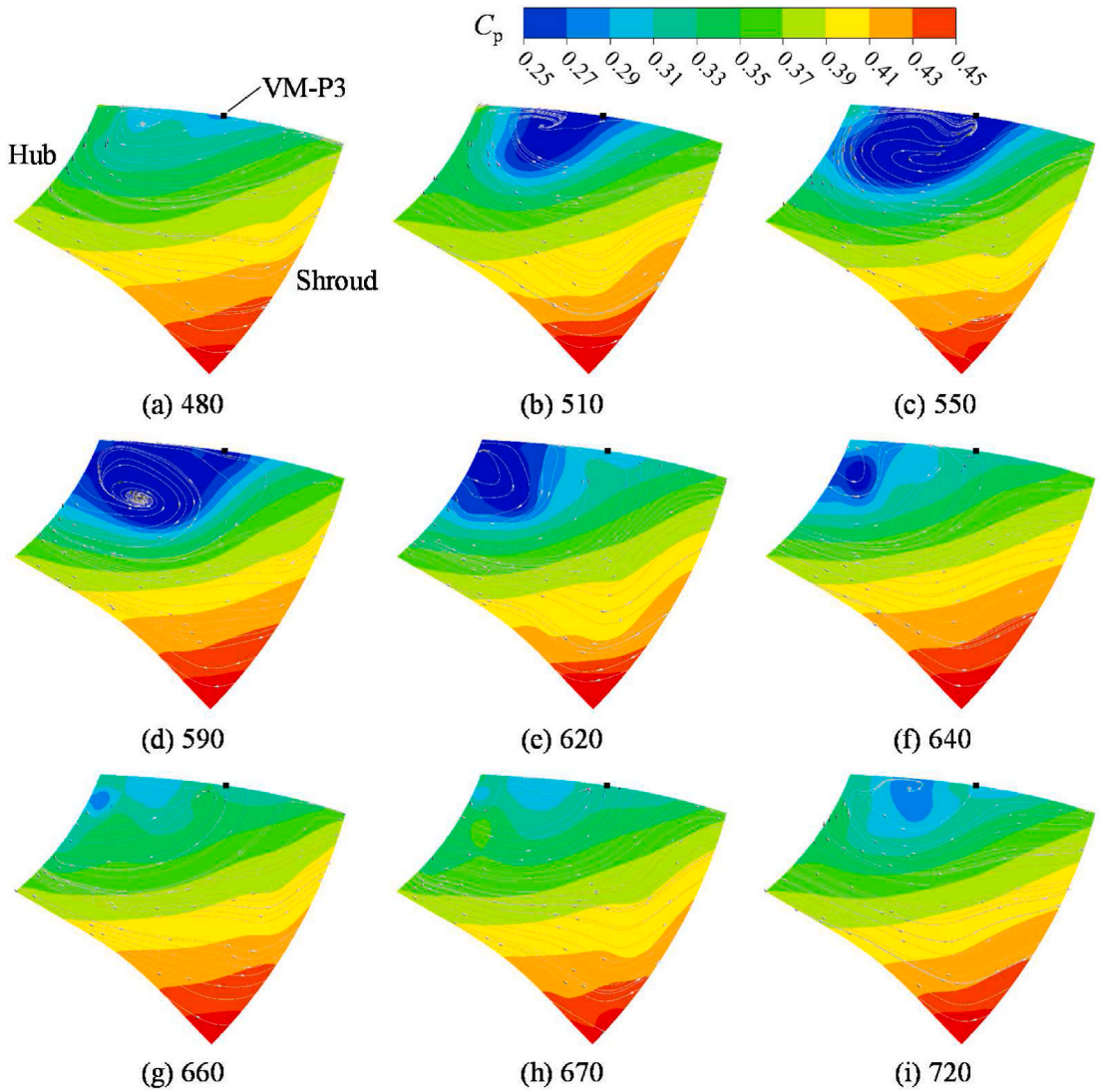

Fig. 13. Instantaneous contours of the pressure coefficient for *dynamics 1* at Case 3 (V_s = 17 m/s).

2400, labeled *dynamics 2*.

Fig. 13 depicts the instantaneous internal flows for *dynamics* 1 by showing the pressure contours overlaid with the streamlines on a cross-section through the point VM-P3. In general, the pressure is high near the vane pressure side (PS) and it is low near the vane suction side (SS), so this pressure gradient in the vane passage would cause a velocity curl on the cross-section plane. In Fig. 13(a), a low-pressure region is initiated around the point VM-P3 with a corner vortex at timestep = 480. Subsequently, the low-pressure region is enlarged starting from timestep = 510 and reaches the maximum at timestep = 590 with an obvious corner vortex. During timestep = 590–640, the low-pressure region is gradually reduced as well as the corner vortex, and they disappear at timestep = 660. Both the low-pressure region and the corner vortex are observed again at timestep = 720. Therefore, the flow field on the cross-section is varied periodically with the evolution cycle of $2/3T_n$, that is, the evolution frequency is $1.5f_n$, which is in accordance with the results obtained by the FFT and wavelet method.

Fig. 14 illustrates the instantaneous flows for *dynamics* 2 by showing the pressure contours overlaid with the streamlines on a cross-section through the point VM-P3. In Fig. 14(b), a low-pressure region is initiated around the point VM-P3 with a corner vortex at timestep = 1970, and then the low-pressure region is enlarged to a very strong vortex at timestep = 2040. Subsequently, the corner flow in the low-pressure region breaks into two vortical structures during 2040<timestep<2160. The vortical structure reaches the maximum at timestep = 2160, and then it gradually reduces. When compared to *dynamics 1*, the flow field is much complex for *dynamics 2* with more vortical structures, causing a $3.0f_n$ frequency in the time-dependent frequency spectra which can only be captured by the wavelet method.

Fig. 15 shows the time histories of the $1.5f_n$ frequency at various monitoring points at V_s = 17 m/s (Case 3). It is in the downstream direction from the point CW3 to CW1, from IM-P1 to IM-P4, and from VM-P1 to VM-P4 in the legend. The $1.5f_n$ frequency fluctuates wildly over time at VM-P3, VM-P4 and IM-P1. The largest amplitude is 0.0794 for VM-P3 at timestep = 618, it is 0.0333 for VM-P4 at timestep = 709, and it is 0.0356 for IM-P1 at timestep = 3600. The mean amplitude is 0.0313, 0.0163, 0.0137 for VM-P3, VM-P4 and IM-P1, respectively.

As for the points CW1, CW2, CW3, IM-P4, VM-P1 and VM-P2, the $1.5f_n$ amplitude fluctuates slightly, and the amplitude is close to each other with the maximum value below 0.0115. It is noted that the amplitude of $1.5f_n$ frequency is very small for monitoring points in the intake duct (i.e. CW1, CW2, CW3), and the mean amplitude is 1.28×10^{-3}, 3.80×10^{-4} and 1.76×10^{-4} at CW1, CW2 and CW3, respectively. On the other hand, the mean amplitude of the $1.5f_n$ frequency for IM-P4, VM-P1 and VM-P2 is 2.62×10^{-3}, 3.20×10^{-3}, 1.82×10^{-3}, respectively.

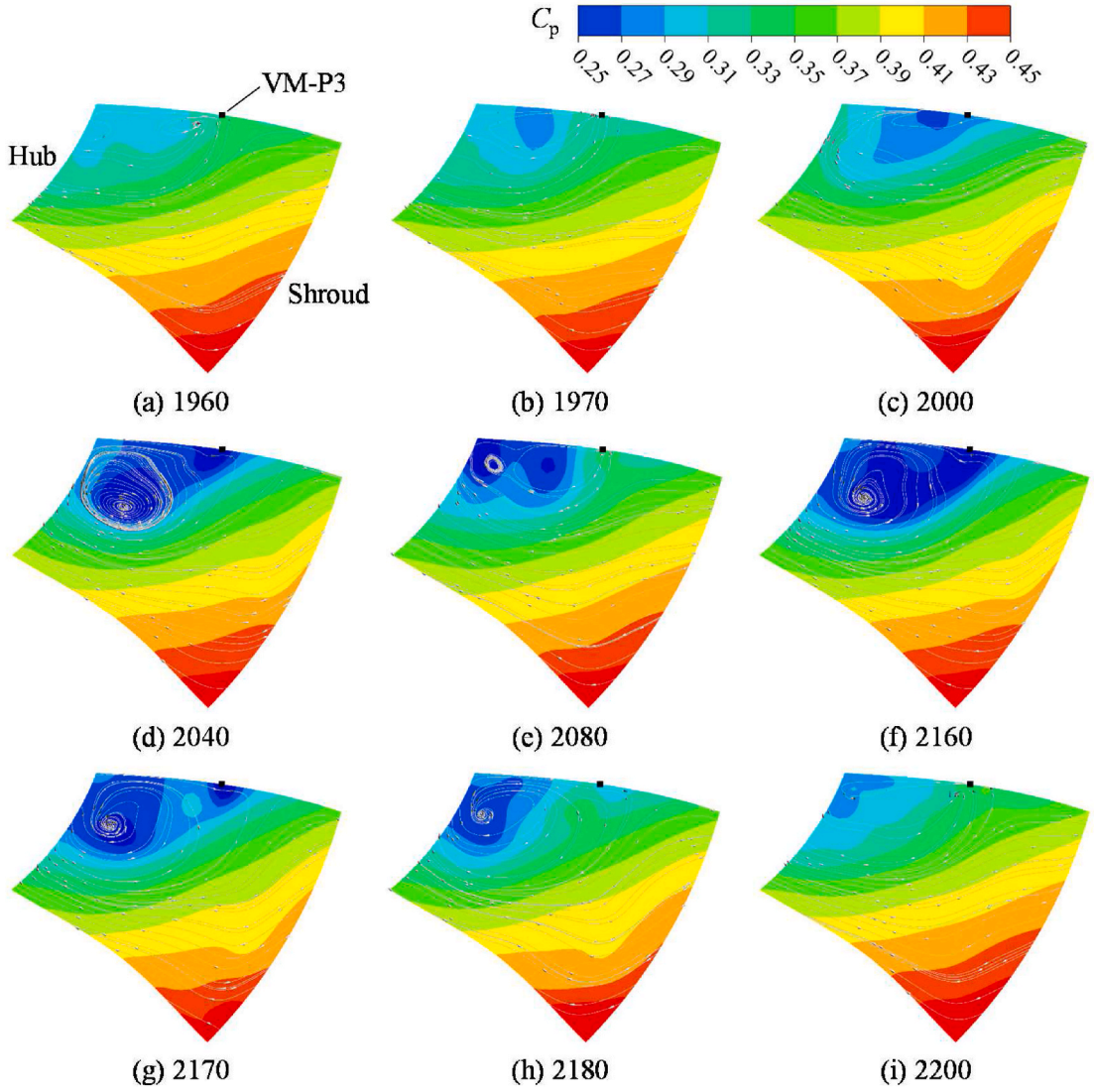

Fig. 14. Instantaneous contours of the pressure coefficient for *dynamics 2* at Case 3 (V_s = 17 m/s).

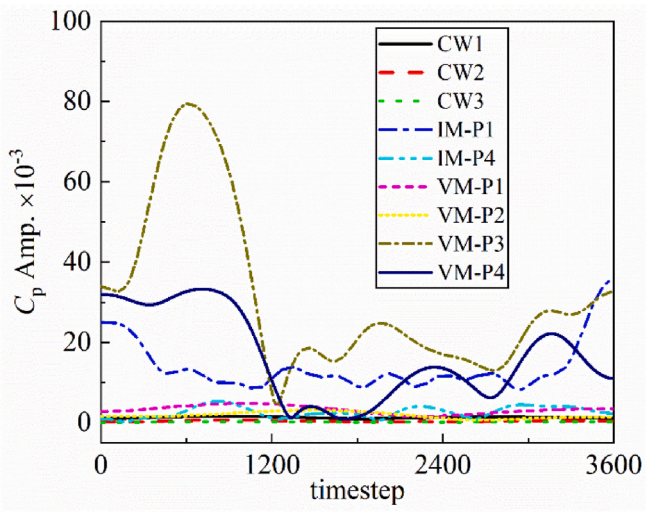

Fig. 15. Time histories of 1.5f_n frequency at various monitoring points at V_s = 17 m/s (Case 3).

Based on the propagation characteristics of the 1.5f_n frequency, it is found that this broadband 1.5f_n frequency originates from the nonuniform outflux with the highest amplitude at VM-P3 and is clarified by *dynamics 1*, which is also reported by Chini et al. (2005). Therefore, this broadband low-frequency found in our numerical simulation is physically explicable, and more physics are explained in (Huang et al., 2020c; Luo et al., 2020).

3.3. The frequency spectra under different cavitation states

The frequency spectra under different cavitation states are discussed herein.

Fig. 16 shows the cavity features at several typical instants during one rotation cycle. Although the operating velocity (V_s) is different, blade 1 is located at the same position expressed by the angle θ between the leading edge of blade 1 and the *y*-axis in the absolute coordinate system. It is demonstrated that there are two stages during one rotating cycle, i.e. the cavity growth stage and the cavity diminution stage.

For V_s = 17 m/s (Case 3), the cavity is a small amount at θ = 9–49°, and then starts to grow along the blade tip in the streamwise direction during θ = 89–289°. The cavity develops to the maximum length at θ = 289°. Subsequently, the cavity starts to shrink and decrease in the length at θ = 339°.

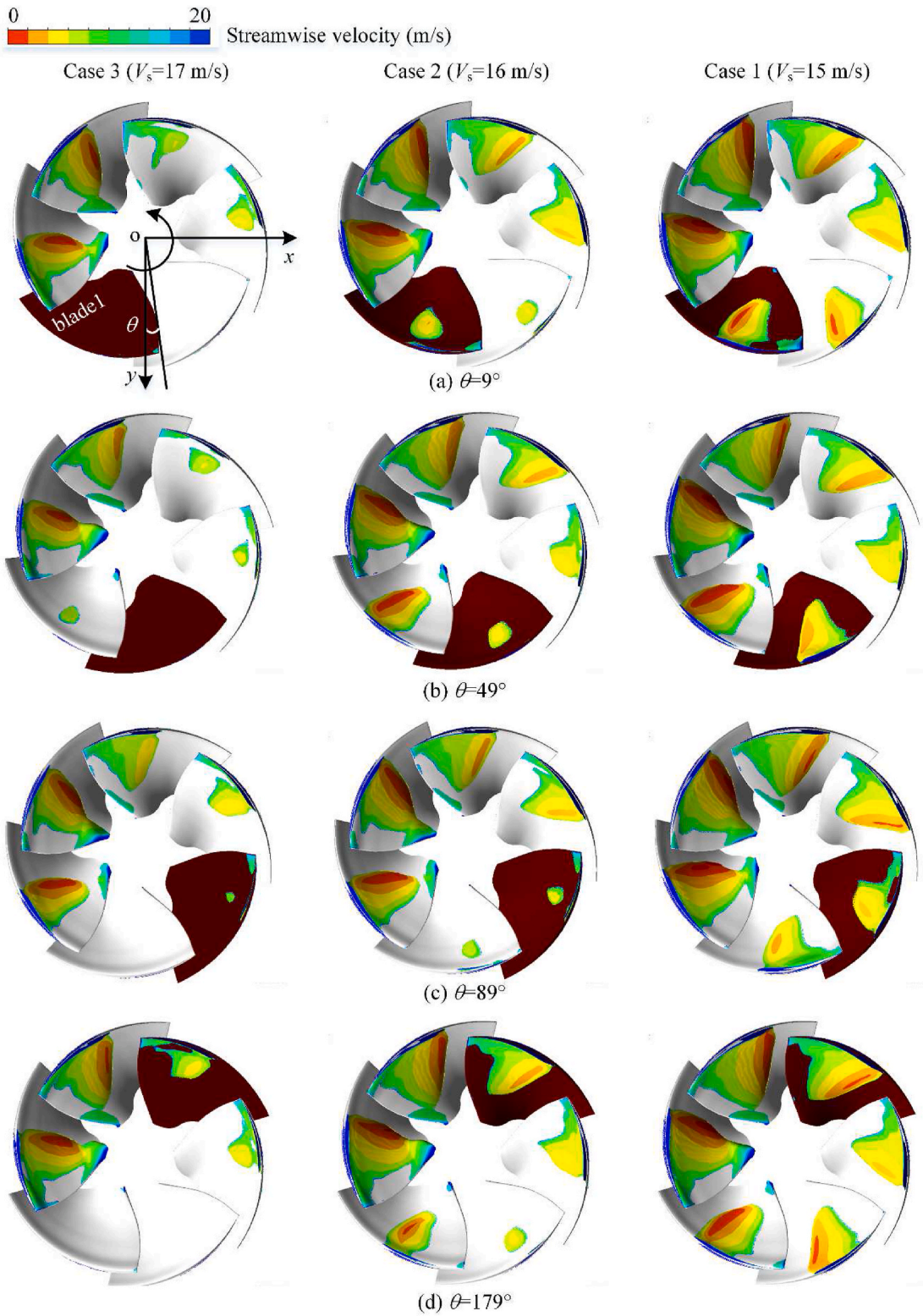

Fig. 16. Comparisons of cavity patterns at typical instants.

For $V_s = 16$ m/s (Case 2), the cavity is observed to decrease from $\theta = 9°$ to $\theta = 49°$ and keep almost the same at $\theta = 89°$. Next, the cavity starts to increase in the cavity length until to the maximum at $\theta = 289°$, and gradually diminishes at $\theta = 339°$.

For $V_s = 15$ m/s (Case 1), the cavity is reduced a little bit from $\theta = 9°$ to $\theta = 49°$, and gradually increased during $\theta = 89°$–$289°$, followed by the reduction at $\theta = 339°$.

Fig. 17 shows the variations of the cavity volume around blade 1 for three cases listed in Table 1, indicating that the tendency of cavity volume around blade 1 (V_c) is similar in different cases, which is gradually increased to the maximum value and subsequently decreased. With decreasing the operating velocity (V_s), the cavity volume around blade 1

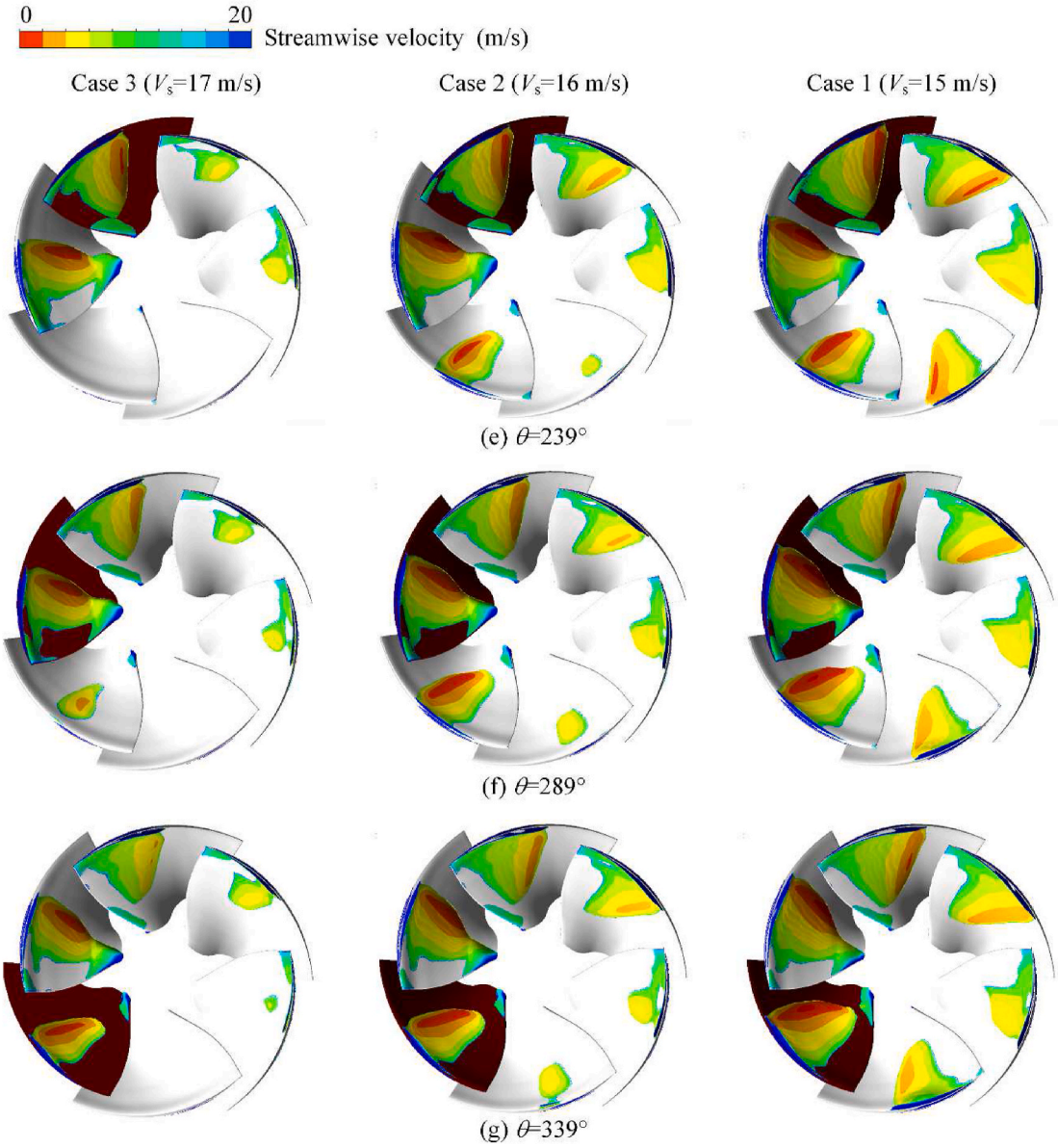

Fig. 16. (*continued*).

is increased, indicating the cavitation becomes more serious.

The non-uniform cavitation evolution features are clarified by using the pressure distribution at the impeller inlet plane as shown in Fig. 18 and Fig. 19, where the reference pressure is set as the saturated pressure in equation (33).

For a specified rotational speed, the circumferential velocity is larger at the shroud than that at the shaft, and thus the static pressure is generally smaller at the shroud than that at the shaft. Besides, the hull boundary layer at the duct inlet would cause the non-uniform energy distribution at the impeller inlet, that is the high-energy fluid is below the shaft and the low-energy fluid is above the shaft. Due to their combined effects, the pressure is high near the rotating shaft, gradually decreases along the radial direction and finally reaches the minimum pressure at the shroud, as shown in Fig. 18. With the operating velocity decreasing from V_s = 17 m/s (Case 3) to V_s = 15 m/s (Case 1), the pressure decreases on the whole, demonstrating the cavitation becomes serious and this is validated by the increase in the cavity volume as shown in Figs. 16 and 17.

The pressure coefficient is extracted from four circular curves at the impeller inlet plane to quantify the spatial non-uniform distribution. As shown in Fig. 19, the pressure is not uniform in circumferential direction at r_1 = 0.046 m and r_2 = 0.065 m, and it fluctuates periodically at r_3 = 0.094 m and r_4 = 0.113 m. Therefore, a high-pressure region presents below the rotating shaft and a petal-like distribution presents along the shroud as shown in Fig. 18(b). The non-uniform pressure distribution in space would affect the cavity patterns in the impeller, that is, the cavity starts to decrease when the blade enters into the high-pressure region and then it develops again when the blade moves out of the high-pressure region.

Fig. 20 shows the frequency spectra of typical monitoring points under different cavitation states. The frequency spectra are obtained by the FFT technique. With decreasing the operating velocity (V_s) from 17 m/s to 15 m/s, the cavitation gradually becomes serious, the frequency distribution is similar and there is only a difference in the amplitude. For the point CW1, the dominant frequency is $6f_n$ with a broadband low-frequency component, and the amplitude is gradually decreased when the cavitation becomes serious in the impeller. Besides, the dominant frequency is f_n at IM-P1 for three cases, which is $6f_n$ at VM-P1 due to the rotor-stator interaction excited by the six-blade impeller. For three cavitation cases, there is a similar broadband low-frequency at the point

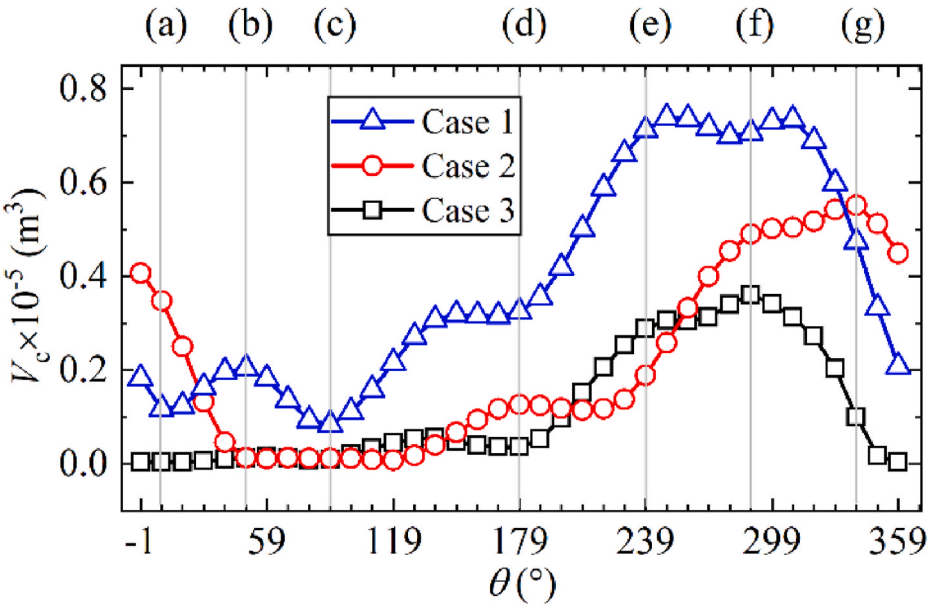

Fig. 17. Time histories of the cavity volume around blade 1 (i.e. V_c).

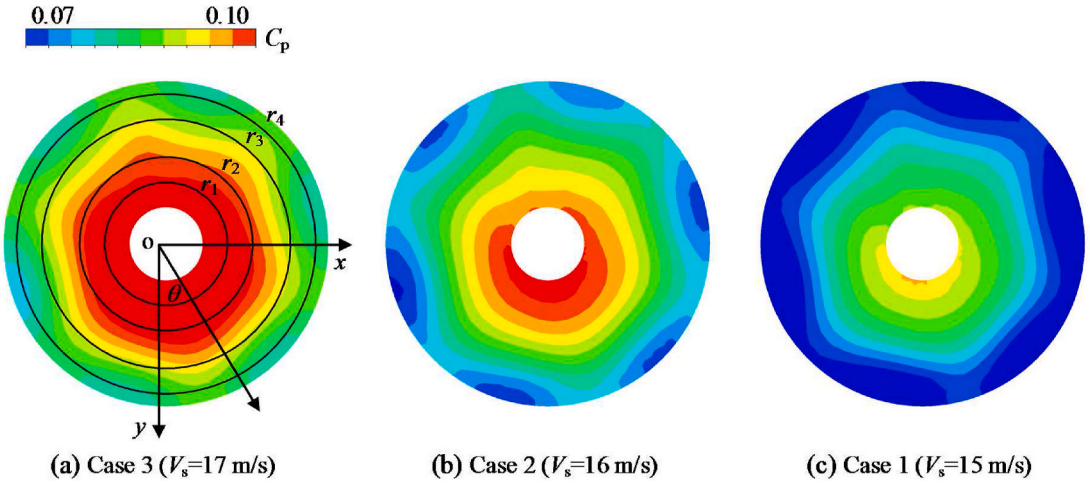

Fig. 18. The pressure distribution at the impeller inlet plane for three cases and the instant corresponds to $\theta = 9°$ as shown in Fig. 16(a).

VM-P3 where the flow is very complicated.

Since the cavitating flow is a multiscale physical phenomenon, the present numerical approach is difficult to obtain microscopic structures inside the cavity, like the single bubble dynamics and the bubble cluster behaviors. However, the selected turbulence model and Zwart cavitation model are sufficiently accurate to simulate the statistical averaged fluid, like the unstable cavity dynamics and the excited pressure fluctuations.

Therefore, as shown in Figs. 19 and 20, when the cavitation becomes more severe, the cavity length increases along the blade streamwise direction, the pressure decreases as a whole, so the monitoring points are likely to be wrapped in the cavity without much pressure fluctuations, causing a decrease in the amplitude of pressure fluctuations.

Fig. 21 depicts the time-varying frequency spectra under different cavitation states.

The dominant frequency at CW1 is a long-term component of $6f_n$, its amplitude is very close at cavitation states, i.e. Case 3 and Case 2. Furthermore, cavitation is the most severe at Case 1, the amplitude is much smaller than that of Case 3 and Case 2. To be specific, the mean amplitude of $6f_n$ component at the point CW1 is 0.00414, 0.0065 and 0.00677 for Case 1, Case 2 and Case 3, respectively. The rotor-stator interaction effect also works at the point VM-P1, so the $6f_n$ component is long-term and has a similar amplitude at three cavitation states. When the cavitation gradually becomes severe from Case 3 to Case 1, the mean amplitude of $6f_n$ component at VM-P1 ranges from 0.0277 to 0.0249.

The dominant frequency in the impeller is $1f_n$ as shown in Fig. 21(b), when the operating velocity decreases from $V_s = 17$ m/s (Case 3) to $V_s = 15$ m/s (Case 1), the cavitation becomes serious inside the impeller, the mean amplitude of the $1f_n$ component gradually decreases from 0.0593 to 0.0483.

There is a broadband low-frequency region at VM-P3, so the typical frequency of $1.5f_n$ is compared among three cavitation states. The $1.5f_n$ amplitude varies over time with one big peak and several small peaks. The largest amplitude at Case 1 is 0.0636 at 3597 timestep, the largest amplitude at Case 2 is 0.0610 at 2787 timestep, and the largest amplitude at Case 3 is 0.0794 at 618 timestep. Although there is difference in the $1.5f_n$ amplitude among three cavitation states, their variation tendency presents a lag in time.

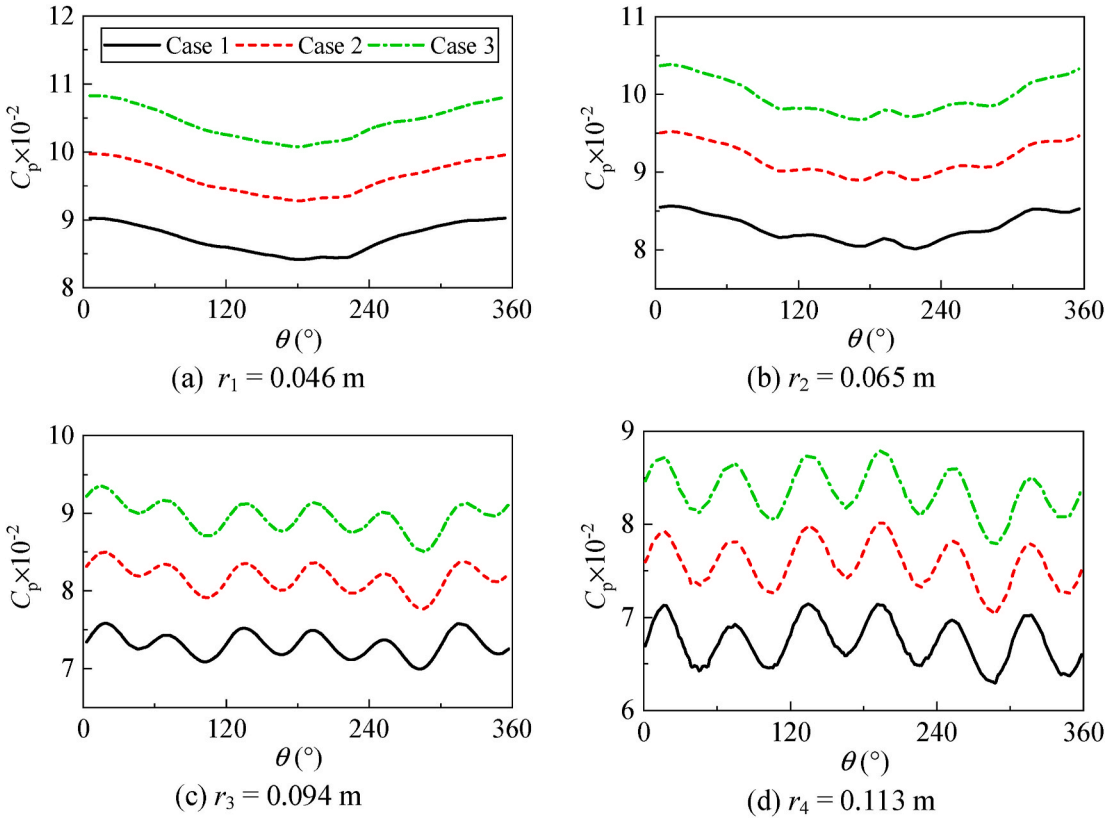

Fig. 19. The pressure coefficient C_p along four circular curves at the impeller inlet plane for three cases and the instant corresponds to $\theta = 9°$ as shown in Fig. 16(a).

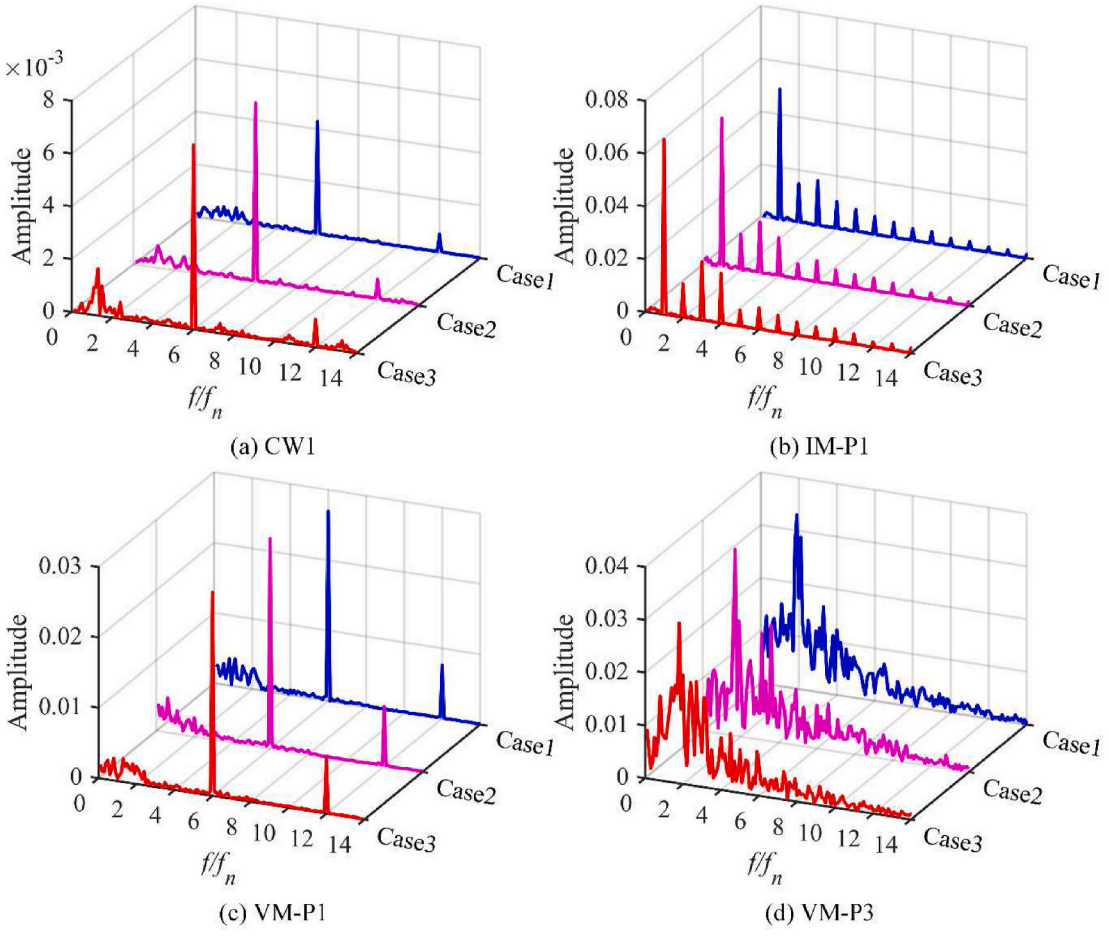

Fig. 20. Frequency spectra analyses under different cavitation states.

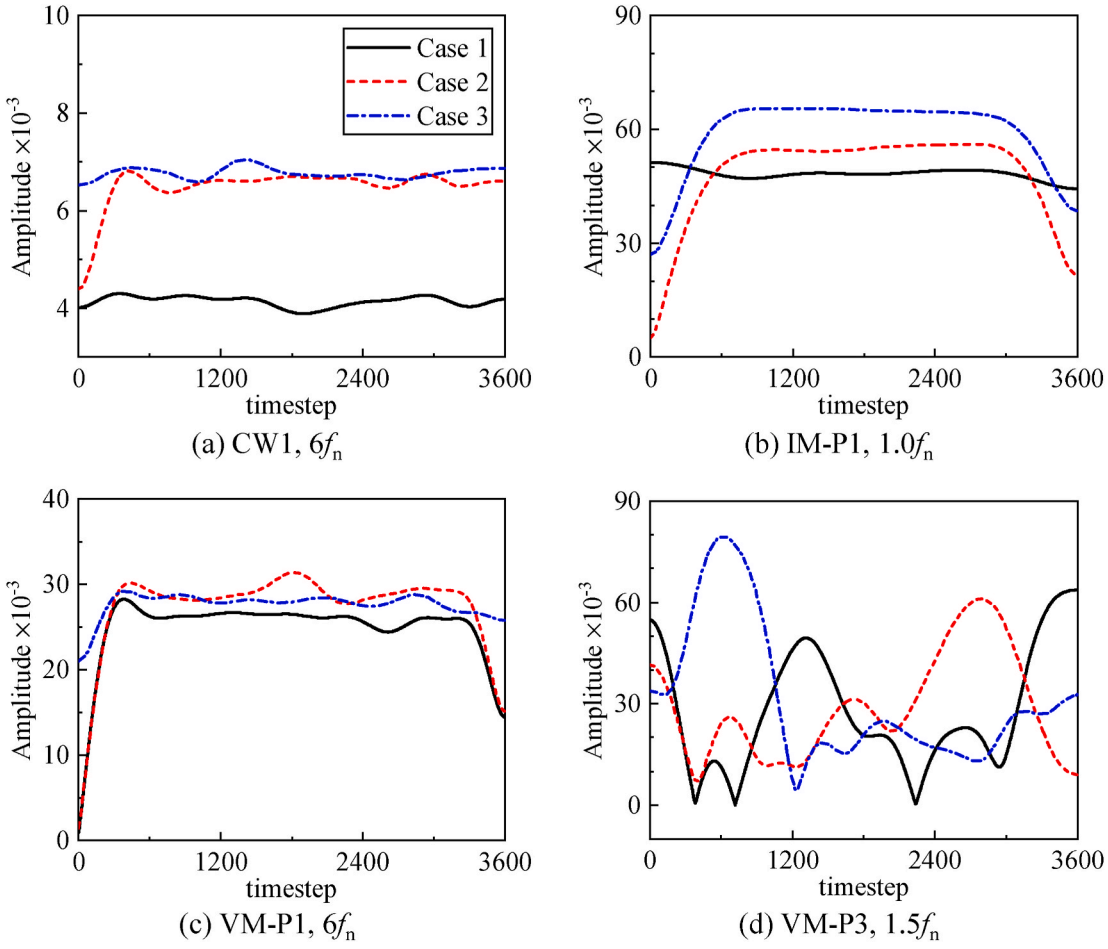

Fig. 21. Time-varying frequency spectra under different cavitation states.

4. Conclusion

In present work, unsteady cavitating flows in a mixed-flow pump are numerically studied in the framework of the Reynolds-averaged Navier-Stokes method, which is closured with the SST k-ω turbulence model and a cavitation model based on the Rayleigh-Plesset equation. The predicted cavitation performance matches well with experimental data. Apart from the Fast Fourier Transform (FFT), a wavelet transform is adopted to analyze the space-time frequency spectra for cavitating flows in a mixed-flow pump. Conclusions are drawn as follows:

(1) Unsteady cavitating flows present two stages during one rotating cycle, i.e. the cavity growth stage and diminution stage, where the cavity volume around blade 1 gradually increases to a maximum and subsequently decreases. The cavitation in the impeller is characterized by the spatial non-uniform distribution since there is a high-pressure region at the impeller inlet plane. A smaller operating velocity (V_s) corresponds to a more serious cavitation state.

(2) FFT analyses show that the dominant frequency at a monitoring point is the same at three cavitation states, while the amplitude of pressure fluctuations overall decreases when cavitation becomes severer at a smaller operating velocity. The dominant frequency in the impeller is the impeller rotating frequency (f_n), i.e. the cavity evolution frequency. A dominant frequency of $6f_n$ exhibits in the intake duct and the diffuser inlet, which is attributed to the rotor-stator interaction from the six-blade impeller. The $1.5f_n$ component originates from the nonuniform outflux in the diffuser with the highest amplitude at VM-P3.

(3) Based on the wavelet analyses, both $1f_n$ and $6f_n$ components are long-term frequencies, and the $1.5f_n$ amplitude varies over time with one big peak and several small peaks corresponding to different corner-vortex dynamics. Although there is difference in the $1.5f_n$ amplitude, their variation tendency presents a lag in time among three cavitation states.

(4) Therefore, the wavelet analysis is acknowledged as a practical method to obtain time-dependent frequency information for unsteady cavitating flows.

CRediT authorship contribution statement

Renfang Huang: Conceptualization, Investigation, Writing – original draft. **Rundi Qiu:** wavelet transform, Methodology. **Yiwei Wang:** Funding acquisition, Supervision. **Xianwu Luo:** Writing – review & editing. **Wei Zhang:** experimental, Resources.

Declaration of competing interest

The authors declare that they have no known competing financial interests or personal relationships that could have appeared to influence the work reported in this paper.

Acknowledgement

The authors would like to gratefully acknowledge the National Natural Science Foundation of China (No. 52006232, 11772340), the Youth Innovation Promotion Association CAS (Y201906), the Science and Technology on Water Jet Propulsion Laboratory (Grant No.

6142223190101).

References

Bardina, J.E., Huang, P.G., Coakley, T.J., 1997. Turbulence Modeling Validation, Testing, and Development.

Brandner, P.A., Venning, J.A., Pearce, B.W., 2018. Wavelet analysis techniques in cavitating flows. Phil. Trans. Math. Phys. Eng. Sci. 376 (2126), 20170242.

Cheng, H., Long, X., Ji, B., Peng, X., Farhat, M., 2020. Suppressing tip-leakage vortex cavitation by overhanging grooves. Exp. Fluid 61 (7).

Chini, S.F., Rahimzadeh, H., Bahrami, M., 2005. Cavitation detection of a centrifugal pump using noise spectrum. In: ASME 2005 International Design Engineering Technical Conferences and Computers and Information in Engineering Conference, pp. 13–19.

Eça, L., Hoekstra, M., Roache, P., 2005. Verification of calculations: an overview of the Lisbon workshop. In: 23rd AIAA Applied Aerodynamics Conference, p. 4728.

Eça, L., Hoekstra, M., Roache, P., 2007. Verification of calculations: an overview of the 2nd lisbon workshop. In: 18th AIAA Computational Fluid Dynamics Conference, p. 4089.

Hao, Y., Tan, L., 2018. Symmetrical and unsymmetrical tip clearances on cavitation performance and radial force of a mixed flow pump as turbine at pump mode. Renew. Energy 127, 368–376.

Huang, H.B., Long, Y., Ji, B., 2020a. Experimental investigation of vortex generator influences on propeller cavitation and hull pressure fluctuations. J. Hydrodyn. 32 (1), 82–92.

Huang, R., Yu, A., Luo, X., Ji, B., Xu, H., 2014. Numerical simulation of pressure vibrations in a Francis turbine draft tube with air admission. In: ASME 2014 4th Joint US-European Fluids Engineering Division Summer Meeting, FEDSM 2014, Collocated with the ASME 2014 12th International Conference on Nanochannels, Microchannels, and Minichannels. American Society of Mechanical Engineers (ASME).

Huang, R.F., Dai, Y.X., Luo, X.W., Wang, Y.W., Huang, C.G., 2019. Multi-objective optimization of the flush-type intake duct for a waterjet propulsion system. Ocean. Eng. 187, 106172.

Huang, R.F., Ji, B., Luo, X.W., Zhai, Z.H., Zhou, J.J., 2015. Numerical investigation of cavitation-vortex interaction in a mixed-flow waterjet pump. J. Mech. Sci. Technol. 29 (9), 3707–3716.

Huang, R.F., Shao, S.Y., Arndt, R.E.A., Luo, X.W., Wang, Y.W., Hong, J.R., 2020b. Numerical study of the behaviors of ventilated supercavities in a periodic gust flow. Journal of Fluids Engineering-Transactions of the Asme 142 (6).

Huang, R.F., Ye, W.X., Dai, Y.X., Luo, X.W., Wang, Y.W., Du, T.Z., Huang, C.G., 2020c. Investigations into the unsteady internal flow characteristics for a waterjet propulsion system at different cruising speeds. Ocean. Eng. 203.

Ji, C., Wang, Y., 2011. The Design and Flow Simulation of the Volute Casing of a Mixed Flow Pump. electronic and mechanical engineering and information technology, pp. 820–823.

Kolahan, A., Roohi, E., Pendar, M.-R., 2019. Wavelet analysis and frequency spectrum of cloud cavitation around a sphere. Ocean. Eng. 182, 235–247.

Lei, T., Zhiyi, Y., Yun, X., Yabin, L., Shuliang, C., 2017. Role of blade rotational angle on energy performance and pressure fluctuation of a mixed-flow pump. Proc. IME J. Power Energy 231 (3), 227–238.

Li, W., Ji, L., Shi, W., Yang, Y., Awais, M., Wang, Y., Xu, X., 2020. Correlation research of rotor–stator interaction and shafting vibration in a mixed-flow pump. J. Low Freq. Noise Vib. Act. Contr. 39 (1), 72–83.

Lilly, J.M., Olhede, S.C., 2009. Higher-order properties of analytic wavelets. IEEE Trans. Signal Process. 57 (1), 146–160.

Liu, H., Chen, X., Wang, K., Tan, M., Zhou, X., 2016. Multi-condition optimization and experimental study of impeller blades in a mixed-flow pump. Adv. Mech. Eng. 8 (6), 1687814016651817.

Liu, M., Tan, L., Cao, S., 2018. Influence of geometry of inlet guide vanes on pressure fluctuations of a centrifugal pump. Journal of Fluids Engineering, Transactions of the ASME 140 (9).

Liu, Y., Tan, L., 2018. Tip clearance on pressure fluctuation intensity and vortex characteristic of a mixed flow pump as turbine at pump mode. Renew. Energy 129, 606–615.

Luo, X., Huang, R., Ji, B., 2016. Transient cavitating vortical flows around a hydrofoil using k-ω partially averaged Navier–Stokes model. Mod. Phys. Lett. B 30, 1550262, 01.

Luo, X., Ye, W., Huang, R., Wang, Y., Du, T., Huang, C., 2020. Numerical investigations of the energy performance and pressure fluctuations for a waterjet pump in a non-uniform inflow. Renew. Energy 153, 1042–1052.

Menter, F.R., 1994. Two-equation eddy-viscosity turbulence models for engineering applications. AIAA J. 32 (8), 1598–1605.

Pan, Z., Li, J., Li, X., Yuan, S., 2012. Performance curve instability and rotating stall. Nongye Jixie Xuebao/Transactions of the Chinese Society of Agricultural Machinery 43 (5), 64–68.

Roache, P.J., 1993. A method for uniform reporting of grid refinement studies. ASME-PUBLICATIONS-FED 158, 109-109.

Vanka, S.P., 1986. BLOCK-IMPLICIT multigrid solution OF Navier-Stokes equations IN primitive variables. J. Comput. Phys. 65 (1), 138–158.

Venning, J.A., Giosio, D.R., Pearce, B.W., Brandner, P.A., 2018. Global mode visualization in cavitating flows. In: Katz, J. (Ed.), Proceedings of the 10th International Symposium on Cavitation (CAV2018). ASME Press, 0.

Wu, Q., Wang, Y., Wang, G., 2017. Experimental investigation of cavitating flow-induced vibration of hydrofoils. Ocean. Eng. 144, 50–60.

Xu, Y., Tan, L., Liu, Y., Cao, S., 2017. Pressure fluctuation and flow pattern of a mixed-flow pump with different blade tip clearances under cavitation condition. Adv. Mech. Eng. 9 (4), 1–12.

Xu, Y., Tan, L., Liu, Y., Hao, Y., Zhu, B., Cao, S., 2018. Pressure fluctuation and flow pattern of a mixed-flow pump under design and off-design conditions. Proc. IME C J. Mech. Eng. Sci. 232 (13), 2430–2440.

Yang, D.D., Luo, X.W., Liu, D.M., Huang, R.F., Zhu, Z.C., 2019. Unstable flow characteristics in a pump-turbine simulated by a modified Partially-Averaged Navier-Stokes method. Sci. China Technol. Sci. 62 (3), 406–416.

Yang, Z., Cheng, Y., Xia, L., Meng, W., Liu, K., Zhang, X., 2020. Evolutions of flow patterns and pressure fluctuations in a prototype pump-turbine during the runaway transient process after pump-trip. Renew. Energy 152, 1149–1159.

Yao, Z., Yang, M., Xiao, R., Wang, F., 2018. Influence of wall roughness on the static performance and pressure fluctuation characteristics of a double-suction centrifugal pump. Proc. IME J. Power Energy 232 (7), 826–840.

Ye, W., Luo, X., Huang, R., Jiang, Z., Li, X., Zhu, Z., 2019a. Investigation of flow instability characteristics in a low specific speed centrifugal pump using a modified partially averaged Navier–Stokes model. Proc. IME J. Power Energy 233 (7), 834–848.

Ye, W.X., Huang, R.F., Jiang, Z.W., Li, X.J., Zhu, Z.C., Luo, X.W., 2019b. Instability analysis under part-load conditions in centrifugal pump. J. Mech. Sci. Technol. 33 (1), 269–278.

Yu, A., Tang, Q., Wang, X., Zhou, D., Liu, J., 2019. Investigation of the pressure fluctuation alleviation in a hydraulic turbine by runner modification. Water (Switzerland) 11 (7).

Yu, A., Zou, Z., Zhou, D., Zheng, Y., Luo, X., 2020. Investigation of the correlation mechanism between cavitation rope behavior and pressure fluctuations in a hydraulic turbine. Renew. Energy 147, 1199–1208.

Zhang, W., Chen, Z., Zhu, B., Zhang, F., 2020. Pressure fluctuation and flow instability in S-shaped region of a reversible pump-turbine. Renew. Energy 154, 826–840.

Zwart, P.J., Gerber, A.G., Belamri, T., 2004. A two-phase flow model for predicting cavitation dynamics. In: Proceedings of the Fifth International Conference on Multiphase Flow, p. 152. Yokohama, Japan.